Insights on the interplay of rifting, transcrustal magmatism and formation of geothermal resources in the central segment of the Ethiopian Rift revealed by 3-D magnetotelluric imaging

M.L.T. Dambly[1], F. Samrock[1], A. V. Grayver[2,3], M. O. Saar[1,4]

[1]Geothermal Energy and Geofluids group, Institute of Geophysics, Department of Earth Sciences, ETH Zurich, Sonneggstrasse 5, 8092 Zurich, Switzerland

[2]Institute of Geophysics and Meteorology, University of Cologne, Albertus-Magnus-Platz, 50923 Cologne, Germany

[3]Earth and Planetary Magnetism group, Institute of Geophysics, Department of Earth Sciences, ETH Zurich, Sonneggstrasse 5, 8092 Zurich, Switzerland

[4]Department of Earth and Environmental Sciences, University of Minnesota, 55455 Minneapolis, USA

Key Points:

- 3-D multi-scale magnetotelluric model imaging the entire transcrustal tectono-magmatic system across a segment of the Main Ethiopian Rift.
- A lower crustal magma ponding zone feeds a fault-aligned magmatic mush column supplying heat for the geothermal system of Aluto volcano.
- Eastern and western volcano-tectonic lineaments likely share a lower crustal magma source with an estimated melt fraction of 7 percent.

Corresponding author: Marie Luise Texas Dambly, mdambly@ethz.ch

Abstract

The Main Ethiopian Rift is accompanied by extensive volcanism and the formation of geothermal systems, both having a direct impact on the lives of millions of inhabitants. Although previous studies in the region found evidence that asthenospheric upwelling and associated decompression melting provide melt to magmatic systems that feed the tectono-magmatic segments in the rift valley, there is a lack of geophysical models imaging these regional and local scale transcrustal structures. To address this challenge, we use the magnetotelluric method and image subsurface electrical conductivity to examine the magmatic roots of Aluto volcano, quantify and interpret the melt distribution in the crust considering established concepts of continental rifting processes and constrain the formed geothermal system. Specifically, we combined regional (maximum $30 \times 120\,\mathrm{km}^2$) and local ($15 \times 15\,\mathrm{km}^2$) magnetotelluric data sets and obtained the first multi-scale 3-D electrical conductivity model of a segment of the central Main Ethiopian Rift. The model unravels a magma ponding zone with up to 7 vol. % melt at the base of the crust ($30 - 35\,\mathrm{km}$ b.s.l.) in the western part of the rift and its connection to Aluto volcano via a fault-aligned transcrustal magma system. Melt accumulates at shallow crustal depths ($\geq 4\,\mathrm{km}$ b.s.l.), thereby providing heat for Aluto's geothermal system. Our model suggests that different volcano-tectonic lineaments in the rift valley share a common melt source. The presented model provides new constraints on the melt distribution below a segment of the rift which is important for future geothermal developments and volcanic hazard assessments in the region.

Plain Language Summary

Continental rifting is a fundamental process of plate tectonics that breaks continents apart to ultimately form new oceans. The landscape of the Main Ethiopian Rift is characterized by abundant volcanism and hot springs, which indicate the presence of geothermal resources formed by magmatic heating of subsurface fluids. Here we present a new 3-D subsurface electrical conductivity image of the magmatic system and geothermal reservoir beneath the Aluto volcano in the Main Ethiopian Rift. The model allows us to estimate the amount and distribution of magmatic melt. This is the first model that provides a high-resolution image of the entire magmatic system below a central part (maximum $30 \times 120\,\mathrm{km}^2$) of the Main Ethiopian Rift from the deep magmatic melt source up to the surface. The new model shows that the geothermal reservoir under Aluto has been formed as a consequence of rifting-related volcanic activity thereby providing a geophysical illustration of fundamen-

tal geological processes. These results also have a high societal relevance by providing a basis for volcanic risk assessment and contributing to a better understanding of how the sustainable green geothermal energy resources form.

1 Introduction

The East African Rift system (EARS) is a prominent continental rift that shaped the landscape of East Africa, including the East African Plateau, rift valleys and numerous volcanoes. Rifting and rift-related volcanism in East Africa played a role in early human evolution (King & Bailey, 2006) and to this date affect the life of humans due to volcanic hazards (Biggs et al., 2021), but also by providing rift-associated natural resources, including geothermal energy resources (Benti et al., 2023; Burnside et al., 2021). A large number of studies, especially in the northern part of the EARS, which includes the Main Ethiopian Rift (MER), have provided a wealth of information and knowledge on the geodynamic processes that initiated and drive rifting and associated volcanism in the EARS (e.g. Agostini et al., 2011a; Casey et al., 2006; Corti, 2009; Courtillot et al., 1999; Ebinger, 2005; Kendall et al., 2005; Kendall & Lithgow-Bertelloni, 2016; Keranen & Klemperer, 2008, and references therein).

One of the main findings of these studies is that neither mechanical stretching nor magmatic upwelling could be the major driver of rifting alone, but it is a rather complex interplay between these processes (e.g. Beutel et al., 2010; Buck, 2004; Kendall et al., 2005). Active magmatism and volcanism in the MER is sustained by asthenospheric upwelling (e.g. Gallacher et al., 2016; Rychert et al., 2012). The main hypothesis is that decompression melting occurs in the upper mantle, melt intrudes into the lithosphere, where it feeds magmatic dykes and sills leading to the formation of volcanic systems in the MER (Chambers et al., 2022; Gallacher et al., 2016; Kendall et al., 2005). Petrological studies and geological mapping (e.g. Hunt et al., 2020; Mazzarini et al., 2016; T. O. Rooney et al., 2011) in the central part of the MER (CMER) observed a spatial correlation between the monogenetic vent distribution and fault systems (Fig. 1), which implies that a tectono-magmatic interplay drives the rifting. Multiple studies proposed that a complex magmatic system with magma stalling and fractionating at multiple depths within the crust exists below the western Silti Debre Zeyit Fault Zone (SDFZ) (Iddon & Edmonds, 2020; Mazzarini et al., 2013; T. O. Rooney et al., 2011). The SDFZ displays only minor surface expressions of faulting (Agostini et al., 2011a) and is a largely aseismic area within the study region (Keir et al.,

2006). In contrast, the eastern Wonji Fault Belt (WFB) has been observed to be seismically more active than the SDFZ (Seismic data from 2001-2003 presented in Keir et al., 2006, Fig.4), hosting the present-day crustal extension with well-developed magmatic pathways (Corti et al., 2020; Mazzarini et al., 2016, 2013; T. O. Rooney et al., 2011). Under the WFB magma rises faster compared to the SDFZ and fractionates at low pressures corresponding to about 5 km depth (M. L. Gleeson et al., 2017; Iddon & Edmonds, 2020; T. O. Rooney et al., 2011). Along the WFB, long-lived silicic peralkaline volcanoes are found with shallow magma chambers that have undergone several phases of eruption and recharge (Fontijn et al., 2018). Active magmatism and extensional strain along the WFB created ideal geological conditions for the formation of high-temperature geothermal resources (e.g. Jolie et al., 2021).

However, geophysical subsurface models constraining the distribution of melt and imaging magmatic pathways across the continental crust within the MER and rifts in general are scarce (e.g. Brune et al., 2023). Such geophysical subsurface images are critical for understanding the controls on magma transport, magma emplacement under rift-aligned segments and the formation of numerous magma-driven geothermal systems in the MER (e.g. Benti et al., 2023; Jolie et al., 2021). The utilization of these geothermal resources would be beneficial for the local society (IRENA, 2020). As a source of clean and renewable baseload energy, these geothermal resources can satisfy the growing energy demand and sustain the local economic growth. Numerous countries along the EARS plan to expand exploitation of renewable geothermal energy resources (IRENA, 2020). Ethiopia is currently aiming at installing 1000 MWe of its estimated 10.000 MWe geothermal energy potential (Benti et al., 2023; Burnside et al., 2021).

Our study focuses on the area of Ethiopia's only energy-producing geothermal power plant, Aluto-Langano. The power plant is in operation since 1998 and has an installed capacity of 7.3 MWe (Benti et al., 2023). Expansion work to reach 75 MWe is underway, with four new wells having been drilled in 2022 (capitalethiopia.com, 2022). Our primary goal here is to investigate the magmatic heat source of Aluto's geothermal system and how it is connected to a deeper lower crustal magmatic system. To this end, we use the magnetotelluric (MT) method and image the 3-D electrical conductivity structure of the subsurface.

Previous MT and seismic studies from this region have respectively identified electrical conductivity and shear wave velocity anomalies in the lower crust under the SDFZ (Hübert et al., 2018; Kim et al., 2012; Samrock et al., 2015). The lower crustal seismic anomalies have been interpreted as a lithospheric melt ponding zone. However, the lateral extent of this anomaly and potential links to Aluto's magmatic reservoir under the WFB remain poorly constrained. Further, it remains unclear whether volcanoes along the Wonji Fault Belt and the Silti Debre Zeyit Fault Zone (Fig. 1) share a common-melt ponding zone or whether their magmas originate from separated parental melt sources (T. O. Rooney et al., 2011).

Our goal is to address these questions and resolve both the regional-scale structures in the lower crust and the local structures related to Aluto's upper crustal magmatic and geothermal reservoirs. To image these structures that span multiple scales, we analyze an MT dataset that covers a segment of maximum 30 km along and 120 km across the rift valley, encompassing the Aluto volcanic complex. Investigating the regional geology in this rift segment provides crucial information on the state of rifting in the central MER, which is considered to be exemplary for a continental rift hosting evolutionary stages between rift initiation and incipient continental break-up (e.g. Agostini et al., 2011a; Brune et al., 2023).

2 Method and Data

We obtain the subsurface 3-D electrical conductivity distribution employing the (passive) magnetotelluric (MT) method (Berdichevsky & Dmitriev, 2008; Chave & Jones, 2012). Broadband MT responses are sensitive to electrical conductivity structures across a wide range of length scales, providing a unique opportunity to study the subsurface from the near surface and through the crust and upper mantle. More details on the MT method are provided in the Supplementary Information (SI) (SI: Text S1).

2.1 Data

We combine data from regional and local MT surveys in the CMER, as is shown in Fig. 1. The regional dataset, collected within the RiftVolc Project (Hübert & Whaler, 2020), consists of 33 MT stations that are distributed across the rift along a profile of $\approx$ 120 km length and two profiles of $\approx$ 32 and 60 km length with average site spacings between 4 km and 13 km (SI: Tab. S1). These regional-scale MT survey was supplemented by a local

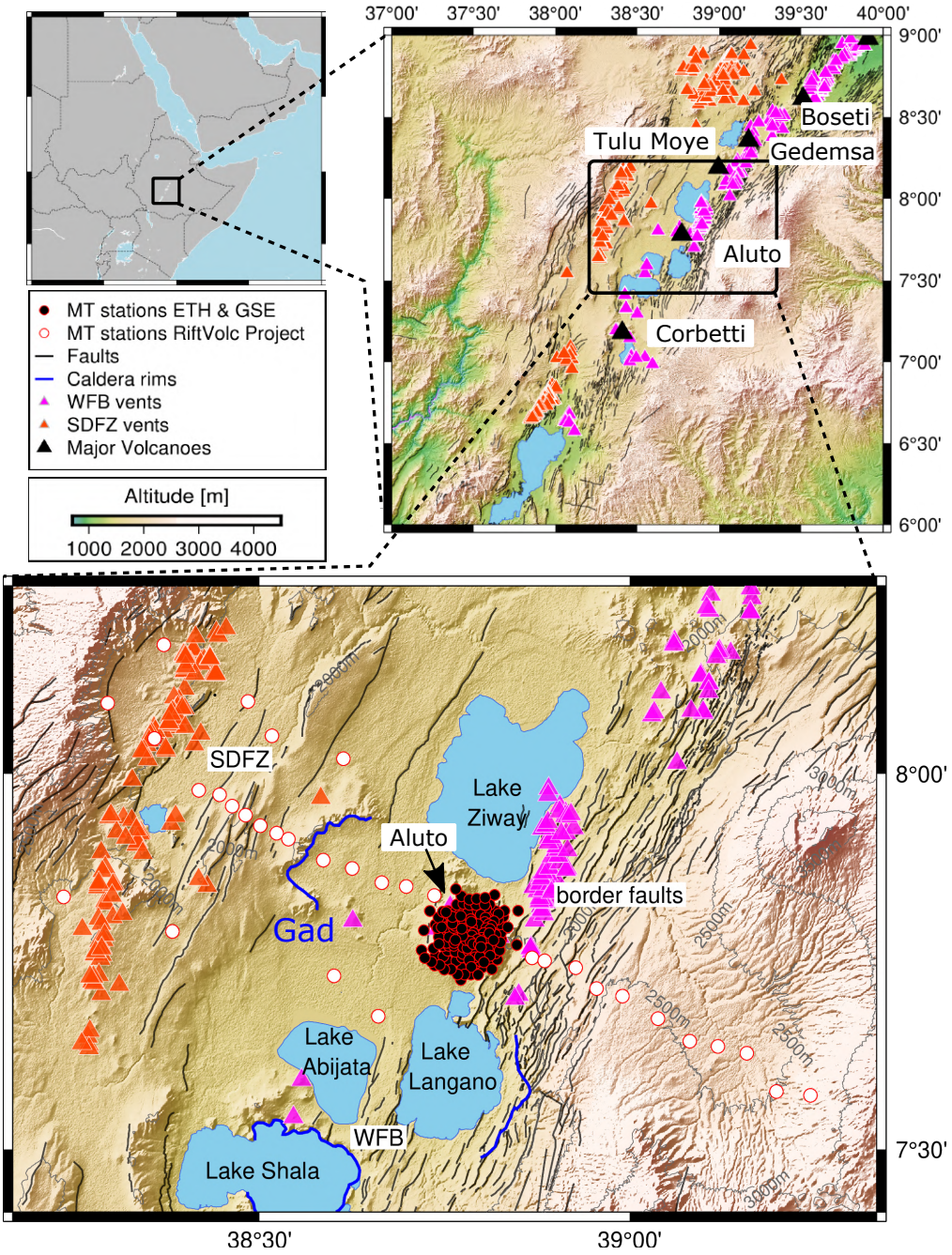

Figure 1. Maps of the study area within East Africa (upper left) and the Main Ethiopian Rift (upper right) within the East African Rift. The lower map presents the study area in the Central Main Ethiopian Rift with its fault systems (database of faults: Agostini et al., 2011b) and quaternary vents (grouped by Mazzarini & Isola, 2010). The vents belong to two different volcanic belts that are associated with the Wonji Fault Belt (WFB) and the Silti Debre Zeyit Fault Zone (SDFZ). Aluto volcano is located in the center of the study area in between the lakes Ziway and Langano. MT stations are coloured according to the institutions and projects that performed the measurement (MT-dataset by ETH Zurich (ETH) and Geological Survey of Ethiopia (GSE): Samrock et al. (2010) and MT-dataset by the RiftVolc Project: Hübert and Whaler (2020)). The survey area encompasses all fault systems of the CMER (WFB, SDFZ and border faults) and crosses the Gademotta caldera rim west of Aluto. The maximum difference in altitude along the profile is $\approx 1000\,\mathrm{m}$.

dataset of ETH Zurich and the Geological Survey of Ethiopia (GSE) (Samrock et al., 2010), consisting of 165 MT sites that cover the edifice of the Aluto volcano ($15 \times 15\,\mathrm{km}^2$), with an average site spacing of 0.7 km. The MT transfer functions cover a period range of $T = 10^{-2} - 10^{3}\,\mathrm{s}$. For this period range and for the averaged electrical conductivity distribution in the study area, the penetration depth is calculated to range between approximately 0.5 and 92.5 km, thereby providing a sufficient range for imaging both near-surface and crustal-scale structures (SI: Fig. S2). The wide survey aperture of 120 km and the small average site spacing of 0.7 km at Aluto illustrate the multi-scale nature of the data. The dense site spacing on the edifice of Aluto volcano allows for imaging near-surface structures at shallow depths relevant for geothermal drilling. The wide aperture of the survey that reaches from the western to the eastern rift shoulder, allows also to image regional-scale structures at depths down to the lower crust.

Maps of the phase tensor data, displayed as ellipses at MT stations for representative periods, convey a first impression of the subsurface electrical conductivity structure (Fig. 2). In general, increased phase tensor ellipticity indicates a lateral electrical conductivity contrast and the corresponding strike is given by the direction of their principal axis (with a 90 ° ambiguity). Further, a maximum phase value of $\Phi_{max} > 45\,^{\circ}$ indicates that electrical conductivities increase with depth and skew-values of $\beta > 3^{\circ}$ are characteristic of 3-D subsurface conductivity structures (Booker, 2014; Caldwell et al., 2004). More details on the phase tensor characteristics are provided in the SI (SI: Text S1).

Phase tensor ellipse maps (Fig. 2) indicate that the regional structure of the rift valley is dominated by an increase of electrical conductivity with depth (at $T > 5\,\mathrm{s}$ $\Phi_{max} > 45\,^{\circ}$). Further, one can observe from ellipticity and skew values that the regional subsurface structure in the western rift valley appears to have stronger lateral contrasts and is more complex (3-D) than in the eastern rift valley. The conductivity structure at Aluto is more complex at shallower depths (e.g. $T = 4.97\,\mathrm{s}$), with relatively stronger lateral electrical conductivity contrasts and 3-D structures in the west and below the center of the volcanic edifice. These strong local differences of subsurface structures diminish with depth.

We conclude that the subsurface electrical conductivity structure is more complex in the western rift area with a strong lateral electrical conductivity contrast that is approximately oriented either rift-parallel or rift-perpendicular. This 90 °-ambiguity is inherent to phase tensor ellipses, so that an inversion of the data is needed to further constrain sub-

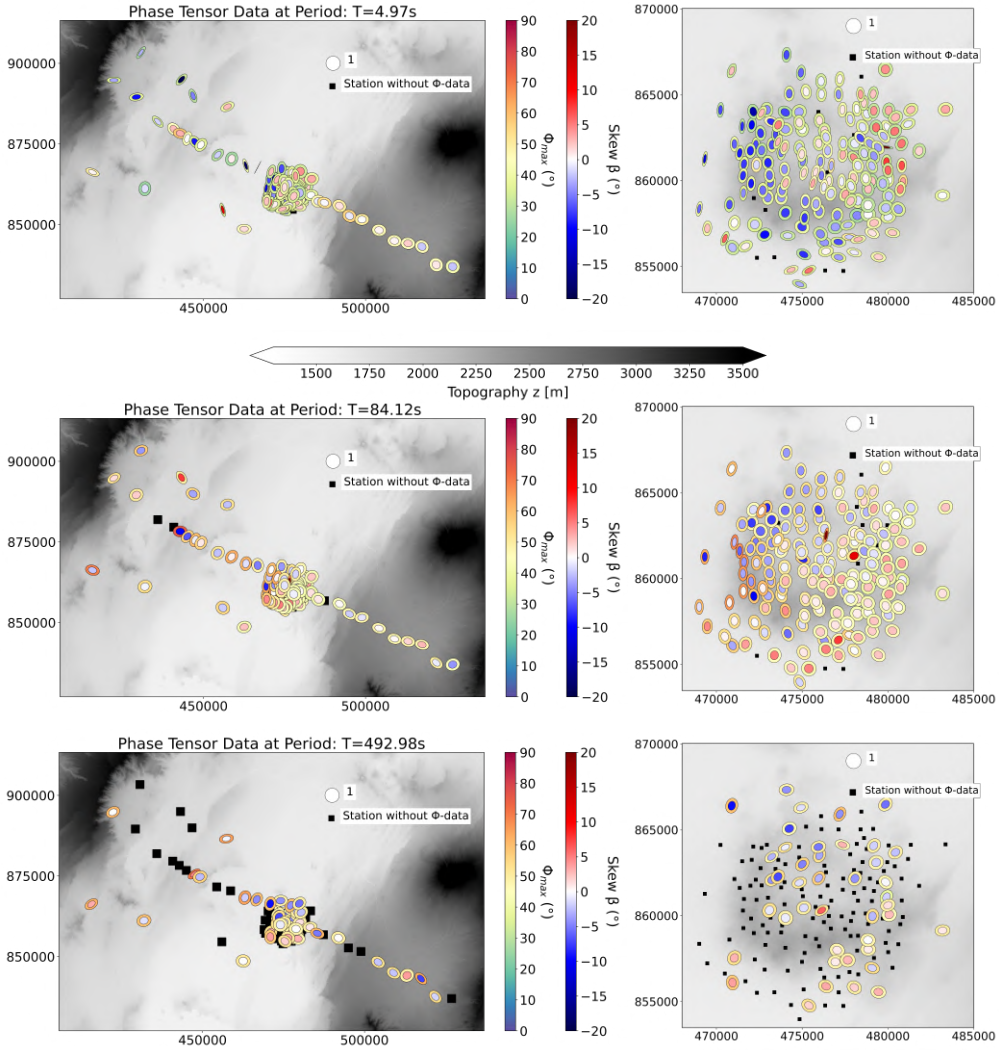

Figure 2. Maps of phase tensor ellipses for different periods at MT stations across the CMER (left) and at Aluto (right) in UTM coordinates. Phase tensor ellipses are normalized by Φ_{max} (see reference ellipse) and coloured by their absolute Φ_{max}-value. The inner core of the ellipses is coloured by the skew (β). Stations that do not have phase tensor data at specific periods due to quality-guided data selection are marked by black squares.

surface conductivity structures. More detailed information on the surveys and the collected MT data is provided in the SI (Text S2).

2.2 3-D Inversion

We use the GoFEM code to perform 3-D forward modelling and inversion (Arndt et al., 2020; A. V. Grayver, 2015; A. V. Grayver & Kolev, 2015). GoFEM uses locally refined meshes to facilitate multi-scale model parameterization (SI: Text S4) and accurately incorporates topography. The code was already used in earlier local-scale MT studies at

Aluto (Samrock et al., 2020) and for multi-scale MT studies of volcanically active regions in Mongolia (Käufl et al., 2020).

Since impedance tensors are often affected by galvanic distortions, we first perform a phase tensor inversion. As the starting model for the phase tensor inversion, we use a homogeneous model with an electrical resistivity of $\bar{\rho}^{1D}_{a,ssq} = 19.25\,\Omega$m, where $\bar{\rho}^{1D}_{a,ssq}$ is the geometric mean of all observed apparent resistivities calculated from Z_{ssq} (SI: Eq. 6-11, see also Rung-Arunwan et al., 2016). We also test phase tensor inversion runs using different homogeneous starting models with arbitrary higher resistivities ($\rho = 25, 35, 50\,\Omega$m). The general observation was that starting models with higher electrical resistivities lead to worse convergences and poorer data fit during phase tensor inversion, proving that choosing a data-informed starting model with an electrical resistivity of $\bar{\rho}^{1D}_{a,ssq}$ is an adequate choice.

Although phase tensors are free of galvanic distortions (e.g. Caldwell et al., 2004), absolute values of electrical conductivities in models constrained solely by phase tensor data are less constrained, especially when the survey layout is sparse (Tietze et al., 2015). To mitigate this limitation, we run the impedance tensor inversion and use the best-fitting 3-D phase tensor model as a starting model. By doing so, the impedance tensor inversion is guided by the distortion-free phase tensor model and the negative impact of galvanic distortions on the inversion is reduced. If there were no distortions and both phase and impedance tensors contained the same information, we would expect the models to be identical. In reality, the models exhibit some differences, mostly because the impedance tensor inversion needs to compensate for galvanic distortions by introducing some scattered conductivity structures at shallow depths (Fig. 2 Samrock et al., 2018) (SI: Fig. S12). We stress that all structures described in the next section appear in all inversion runs and thus represent robust conductivity anomalies required by data.

Technical information on the inversion methodology and the achieved data fit for the final phase and impedance tensor models is provided in the SI (Text S3 and S4). In what follows, we present the final impedance tensor model. The corresponding phase tensor model is shown for completeness in the SI (Text S4.1).

3 Results

Both models, obtained from phase and impedance tensor inversions, fit the observed data within the uncertainty (RMS$\leq$1), given by the error-floor of 5 % applied row-wise to the

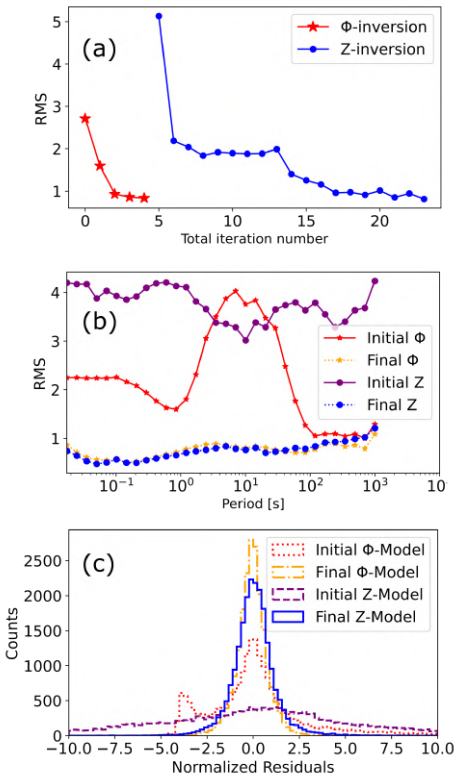

Figure 3. (a) RMS misfit during the phase tensor and the subsequent impedance tensor inversions. (b) RMS misfit versus period for the initial and final phase and impedance tensor inversion runs. (c) Residual distribution of initial and final phase tensor and impedance tensor models. Note that the final phase tensor model is used as a starting model for the impedance tensor inversion.

impedance tensor and propagated to the phase tensor (as in Käufl et al., 2018). Details about the inversion progress and the achieved fit are provided in Fig. 3. Starting at an initial RMS of 2.7, the phase tensor inversion converges to an RMS of 0.83 within four iterations. For the subsequent impedance tensor inversion a relatively low model regularization is chosen, as the large-scale structure is given by the phase tensor model, which is used as the starting model for the impedance tensor inversion. Starting at an initial RMS of 5.1, the impedance tensor inversion converges progressively until a final RMS of 0.81 is achieved (Fig. 3a). The RMS distribution as a function of the period shows that shorter periods tend to yield lower misfits than longer periods (Fig. 3b), which can be caused by lower data quality at longer periods. The normalized residuals of both obtained final models are uniformly distributed and centered around zero, indicating that no systematic bias is present (Fig. 3c). More detailed information about the model fit is provided in the SI (Text S5.2).

3.1 Final model

An approximately NW-SE-oriented profile through the final electrical conductivity model is shown in Fig. 4. The presented profile section crosses the entire rift valley and traverses through the center of Aluto volcano. Main electrical conductors (C) in the obtained multi-scale model are described in the following.

The largest electrical conductivity anomaly in the model is the C3 conductor. The maximum recovered electrical conductivity within C3 is $\sigma = 0.18\,\mathrm{S/m}$ (Fig. 4 a). The anomaly occupies a large volume in the lower crust under the western part of the rift and crosses the Moho boundary at depths of $z \approx 30 - 35\,\mathrm{km}$ b.s.l. (Fig. 5, SI: Fig. S17). The lateral extent of C3 is about 50 km across the rift and 30 km along the rift with a maximum thickness of $\approx 15\,\mathrm{km}$, considering the $0.1\,\mathrm{S/m}$ isosurface. However, due to the limitations imposed by the survey layout, the southern extent of the western conductor C3 is not well constrained. In the lower crust under the eastern part of the rift valley no high conductivity zone is imaged. Anomaly C3 terminates at the central rift axis, where a steep dipping conductive channel C2 is imaged. The C2 structure is characterized by increased bulk electrical conductivities of $\sigma = 0.1 - 1.8\,\mathrm{S/m}$ at depths of $z = 6 - 18\,\mathrm{km}$ b.s.l.. This channel terminates at a depth of $z = 4\,\mathrm{km}$ b.s.l. immediately below Aluto volcano (Fig. 4 b). At shallower depths (down to about $z \approx 1.5\,\mathrm{km}$ below the surface), we recover an electrically conductive layer (C1) that extends across the entire width of the rift, with bulk conductivity values of $\sigma = 0.1 - 0.5\,\mathrm{S/m}$. This continuous layer (C1) is interrupted only under the edifice of Aluto volcano in the center of the shown cross-section (Fig. 4).

A large low-conductivity zone (R1) extends across the valley, with $\sigma \leq 0.01\,\mathrm{S/m}$. R1 is situated in the crust below the continuous conductive layer (C1) and is pierced by the conductive channel C2.

3.2 Interpretation

In the following sections, we provide a geological interpretation of the 3-D multi-scale electrical conductivity model (Figs. 4, 5 and 6).

3.2.1 C3: Lower crustal magma ponding zone

To assess whether the conductive anomaly C3 is caused by the presence of electrically conductive magmatic melt, we first refer to the findings of past studies. Volcanic vents

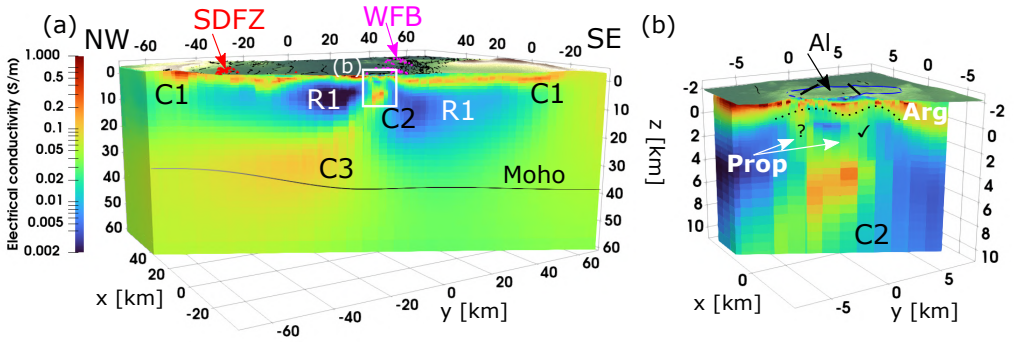

Figure 4. Final 3-D electrical conductivity model. (a) NW-SE oriented cross-section, covering the entire width of the CMER. The Moho boundary (black solid line) is taken from (Stuart et al., 2006). Pink and red triangles depict WFB and SDFZ vents, respectively (see also Fig. 1). Recovered structures are interpreted to be: (C1) Aquifer/sediment unit, (C2) magma ascent channel, (R1) solidified igneous rock and (C3) lower crustal melt ponding zone. The white box marks the area of the Aluto-Langano geothermal system (b). (b) Enlargement of Aluto volcano (proposed caldera rim in blue). Increased electrical conductivities in the shallow subsurface can be attributed to a clay cap, formed by argillic alteration (Arg) and higher-temperature propyllitic alteration (Prop). The dashed line marks the bottom of the clay cap (argillic alteration zone). Note, alteration zones in the east (tick sign) are confirmed by geothermal wells.

above C3 within the western SDFZ tectonic segment hint at past magmatic activity in this region (Fig. 1). The existence of magma within the structure C3 below the SDFZ is further supported by high levels of CO_2 degassing in the area (Hunt et al., 2017). That the SDFZ volcanic segment is fed by magma ponding at the base of the crust has also been suggested by several petrological models (e.g. T. O. Rooney et al., 2011). These petrological models for melt distribution are supported by several geophysical studies. The analysis of seismic S-to-P receiver functions has provided evidence for a thinned lithosphere and an upwelling asthenosphere below the rift valley of the northern MER. Rychert et al. (2012) performed geodynamic modelling, showing that melt generated through decompression melting in the upwelling asthenosphere experiences strong buoyancy forces causing the melt to migrate into the lower crust, where it accumulates in a melt ponding zone above the Moho.

In the central MER, a similarly pronounced low seismic velocity anomaly is observed in the upwelling asthenosphere, which can only be explained by the presence of melt that originates from decompression melting (e.g. Chambers et al., 2022; Kim et al., 2012). This melt-ponding reservoir is spatially coherent with the C3 structure in our model. It has

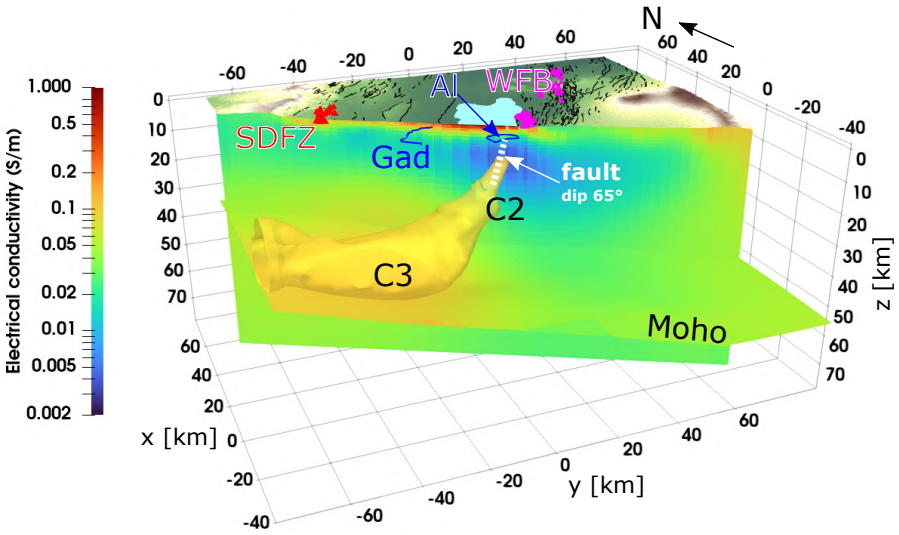

Figure 5. Vertical slice through the final electrical conductivity model, approximately along the northern profile line of the MT sites (see Fig. 1). The Moho, as in Fig. 4, is colored by the electrical conductivities at the corresponding depth. The $\sigma = 0.1\,\mathrm{S/m}$-isosurface illustrates the extent of the magmatic ascent channel (C2) and the lower crustal melt ponding zone (C3). The general dip ($> 65\,^{\circ}$) of faults intersecting Aluto (Al), reported by Corti (2009), is shown as a dashed white line. Vents at the Wonji Fault Belt (WFB) and Silti-Debre Zeyit Fault zone (SDFZ) are represented as red and pink triangles, respectively. The Gademotta (Gad) caldera rim is shown as a blue line, faults as black lines.

further been shown that the Moho deepens from west to east in this area (Fig. 4), indicating that asthenospheric upwelling is slightly asymmetric to the rift axis and more pronounced under the western part of the rift (e.g. Keranen & Klemperer, 2008; Stuart et al., 2006).

The observation that melt is asymmetrically distributed across the rift has also been made by Hübert et al. (2018), who performed a 2-D inversion of the regional RiftVolc MT dataset used in this study (Fig. 1, see SI: Tab. 1). Further comparison between the models is provided in the discussion (Section 4).

In agreement with the results of the above mentioned studies, we conclude that the high electrical conductivity anomaly C3 is caused by the presence of electrically conductive basaltic melt. The lower bound of this melt-enriched area coincides with the depth of the seismic Moho provided by the model of Stuart et al. (2006) (Fig. 5). Our electrical conductivity model suggests that the melt is not distributed uniformly along the imaged lower crustal segment of the SDFZ, but is rather focused in a region spatially confined to

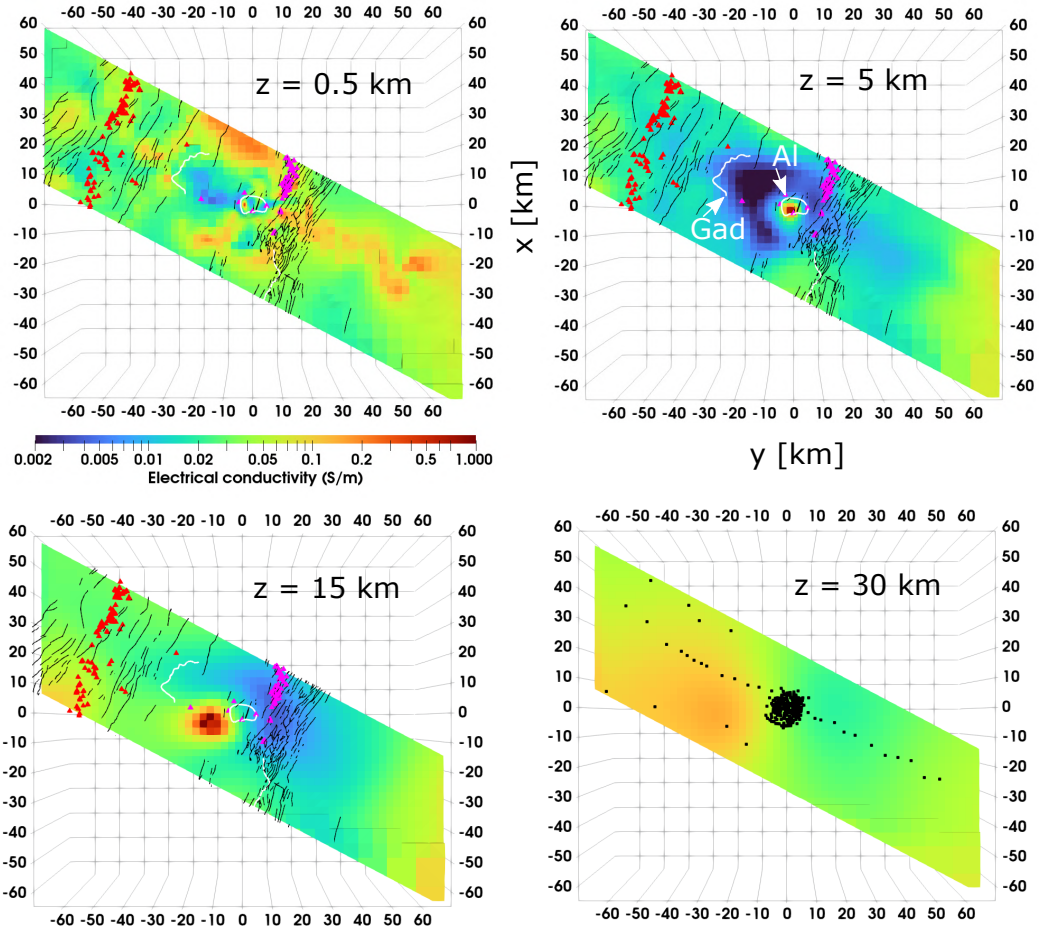

Figure 6. Horizontal slices at several depths from $z = 0.5 - 30$ km b.s.l. through the final impedance tensor model. Pink and red triangles depict WFB and SDFZ vents, respectively, black lines are faults and white lines are the western Gademotta caldera rim and the proposed Aluto caldera rim. Black dots on the 30 km b.s.l. depth slice indicate MT site locations.

the WSW of Aluto (Fig. 5, Fig. 6: z=30 km). The seismic Moho depth is shallower below the western part of the rift (Stuart et al., 2006), suggesting asthenospheric upwelling in this area. Therefore, C3 may represent the magmatic reservoir fed by asthenospheric decompression melting, as predicted by the geodynamic modelling studies conducted by Rychert et al. (2012).

3.2.2 Melt fraction estimates

The model obtained from this study allows us to use electrical conductivity as an independent constraint to quantify the amount of basaltic melt present in the lower crust. Until now, such estimates in the central MER relied mainly on seismic studies (summarized in

the SI, Tab. S2). Adding electrical conductivity reduces uncertainty of melt estimates and places previously lacking bounds on the spatial extent of the melt reservoir. To estimate the melt content, we use the experimental model by Ni et al. (2011) (SI: Text S6), which parameterizes the electrical conductivity of basaltic melt in terms of temperature and dissolved water content. For calculating the basaltic melt conductivity, we assume temperatures of $\mathcal{T} = 1300 - 1400\,^{\circ}\mathrm{C}$ within the interpreted melt source region (C3). The lower temperature bound of $\mathcal{T} = 1300\,^{\circ}\mathrm{C}$ is defined by the minimum temperature, for which the electrical conductivity model by Ni et al. (2011) is valid. The maximum assumed temperature has been reported in the petrological study by T. O. Rooney et al. (2012) as the temperature of parental basaltic melt in the study area (SI: Tab. S2). Thermodynamic modelling of the melt evolution of magmatic rock samples from Aluto constrains the dissolved water content within the parental basaltic melt to $c_{H2O}^{melt} <= 1\,\mathrm{wt\%}$ (M. L. Gleeson et al., 2017). This amount is well below the maximum water solubility of $c_{H2O}^{melt} = 6.7\,\mathrm{wt\%}$ for identical magma storage conditions, which we calculate using the MagmaSat package (Ghiorso & Gualda, 2015).

Under the mentioned conditions (see SI: Tab. S2), the electrical conductivity of basaltic melt is approximately $\sigma_{melt} = 2.9 - 8.4\,\mathrm{S/m}$ (SI: Fig. S14). Based on the basaltic melt conductivity and the observed range of $\sigma_{bulk} = 0.1 - 0.18\,\mathrm{S/m}$ in the magma ponding zone (C3), we calculate the melt fraction, using the modified Archie's law (SI: Eq. 17 Glover, 2015). The melt fraction is estimated for high melt-connectivities, reflected by a cementation exponent of $m = 1.15$, which describes the upper limit of effective porosities in a two-phase material (Pommier & Garnero, 2014), and lower connectivities, reflected by $m = 1.5$, which corresponds to interstitial melt storage in a matrix of closely packed, perfect spheres (e.g. Glover, 2015). With these constraints, the melt fraction within the C3 conductor is $1.8 - 7.1\,\mathrm{vol.\%}$ and $4.5 - 14.7\,\mathrm{vol.\%}$ for maximum and minimum conductivities of the basaltic melt, respectively. Previous estimates from seismic tomography predicted $2 - 7\,\mathrm{vol.\%}$ of vertically aligned melt (J. O. Hammond & Kendall, 2016, SI: Tab. S2). Compared to these numbers, our maximum melt fraction estimate of $14.7\,\mathrm{vol.\%}$ appears rather high. To put it in context, a melt fraction of $14.7\,\mathrm{vol.\%}$ is even higher than MT-based estimates from the Dabbahu magmatic segment in the Afar region (Desissa et al., 2013, SI: Tab. S2). There, dyking maintains extension of the crust (Wright et al., 2006; Manighetti et al., 1998) and the crust is generally thinner (Fig. 3, 4 in Keranen & Klemperer, 2008, and references therein). In Afar, rifting is far more advanced as when compared to the central MER (Bonini et al.,

2005; Manighetti et al., 1998; Hayward & Ebinger, 1996; Barberi & Varet, 1978). Therefore, the connectivity model leading to the maximum melt fraction of 14.7 vol.% is rather unrealistic. Instead, higher temperatures, water contents and enhanced melt connectivity are the conditions that better describe the in situ settings. In this case, our estimated melt fraction range is $1.8 - 7.1$ vol.%. These melt fractions are in agreement with estimates derived from seismic velocity models (see SI: Tab. S2) and support the interpretation of the C3 conductor as a lower crustal magma ponding zone.

3.2.3 C2: Transcrustal magma ascent channel

We interpret the upward rising conductor C2 to be the magma ascent channel in which melt migrates from the deeper melt ponding zone (C3) to the shallow magmatic system beneath Aluto (Fig. 5, 6). The enhanced electrical conductivity of C2 requires that partial melt is present in the channel up to depths of ≈3 km b.s.l.. Hence, the upper part of C2 also represents the magmatic heat source of Aluto's geothermal reservoir (Fig. 4 b). Previous petrological studies (Mazzarini et al., 2013; T. O. Rooney et al., 2011; T. Rooney et al., 2007) have characterized magma ascent channels below the Wonji Fault Belt to be 'mature' and to enable 'quick' magma ascent as they found evidence that magma fractionation does not happen throughout the crust, which implies developed magmatic pathways. According to these studies, magma either stalls and fractionates at shallow depth (≈ 1 kbar) and partially erupts as rhyolite, or the melt erupts as basalt without undergoing melt fractionation (Mazzarini et al., 2013; T. O. Rooney et al., 2011; T. Rooney et al., 2007). The imaged anomaly C2 reconciles with this concept since increased electrical conductivities indicate that small magma fractions exist throughout the channel. Therefore, C2 likely delineates a complex system of magmatic pathways, which assists new magmatic recharge.

Another evidence for melt being present within C2 beneath Aluto is its spatial correlation with an observed aseismic zone (SI: Fig. S18) that was interpreted as hot ductile crust by Wilks et al. (2017, 2020). The shallower part of the C2 structure has already been described by the previous studies analysing the local MT dataset at Aluto volcano (Samrock et al., 2021, 2020). These studies highlight that the dip angle of C2 is in agreement with the general dip of $\geq 65\,^{\circ}$ of the faults intersecting Aluto volcano (Corti, 2009). To aid visual illustration, we added this fault plane in Fig. 5. A link between magmatic pathways and fault zones has been described by numerous studies investigating magma-assisted continental rifting (e.g. Casey et al., 2006). The spatial correlation between active tectonic faults

and magma pathways in the central MER is evident from the distribution of vents (Fig. 1) (e.g. Mazzarini et al., 2016; Kendall et al., 2005). Therefore, magma preferentially rises along fault zones, where the crust has been weakened (e.g. Corti, 2008; Mazzarini et al., 2013).

3.2.4 R1: Solidified igneous rock

This electrical resistor has already been imaged by previous MT studies who interpreted it to be cooled intrusive rock (Hübert et al., 2018; Samrock et al., 2020). This interpretation is also in agreement with a Bouguer gravity high in the Gademotta caldera (e.g. Mickus et al., 2007; Nigussie et al., 2023). In our model the minimum electrical conductivity of this resistor is 0.002 S/m, which is in the range of the electrical resistivity of gabbro in the crust (Dai et al., 2015). As in the model by Hübert et al. (2018), the electrical resistor is bounded to the west below the Gademotta caldera rim (see e.g. depth slice at 5 km b.s.l. in Fig. 6). The spatial correlation between intrusive rock and the caldera is not unusual. Calderas form after the emptying of an underlying magma reservoir and do therefore mimic the approximate outline of the magma reservoir as validated in studies about calderas (e.g. Geshi et al., 2014; Geyer et al., 2006). Volcanism at Gademotta ceased 1 Ma ago (Hutchison et al., 2016), providing enough time for the intrusions to crystallize and cool down (e.g. Cawthorn & Walraven, 1998).

3.2.5 C1: Aquifer/sediment unit

Following the conceptual hydrogeological model of the study area (Ghiglieri et al., 2020), the conductor C1 images a shallow layer of pyroclastics and lavas that has been classified as a fissured aquifer. Considering reported groundwater electrical conductivities with a mean of 0.3 S/m in the area (Burnside et al., 2021), the most widely distributed observed bulk conductivities within C1 ($\sigma = 0.1 - 0.2$ S/m) would require an unreasonably large fluid fraction within C1 (see SI: Text S6.2). It is thus likely that enhanced conductivities in C1 are attributed to a superposition of pore fluid conduction and conduction through a conductive soil component such as clays (e.g. Pride, 1994; Qi & Wu, 2022). Clays also form through rock weathering processes and are commonly found in soils around the study area (Fritzsche et al., 2007).

3.2.6 Geothermal system

The shallow cap-like conductor ($\sigma = 0.1 - 0.3\,\mathrm{S/m}$), shown in Fig. 4 b under Aluto volcano down to depths of 1.5 km below the surface, and the underlying zone of decreased electrical conductivities ($\sigma = 0.02\,\mathrm{S/m}$) between the cap and the upper part of the magma ascent channel C2 are typical features of volcano-hosted, high-temperature geothermal systems (e.g. Bertrand et al., 2012; Omollo et al., 2022; Yamaya et al., 2022). The electrically conductive cap represents the argillic alteration zone, where electrically conductive clays are formed along the flow paths of circulating hot fluids on top of the convective hydrothermal reservoir (e.g. Pellerin et al., 1992). These conductive clay minerals dominate at temperatures of $\mathcal{T} \approx 80 - 220\,^{\circ}\mathrm{C}$. The electrically more resistive region under the clay cap represents the propylitic alteration zone, where less electrically conductive alteration minerals, such as chlorite and epidote, form at higher temperatures of $\mathcal{T} > 250\,^{\circ}\mathrm{C}$ (Árnason et al., 2000; Flóvenz et al., 2012; Kristmannsdottir, 1979; Lévy et al., 2018). Updoming of the argillic clay cap indicates updoming of temperature isolines and hence an increased vertical temperature gradient (e.g. Trainor-Guitton et al., 2017). Below Aluto two areas of clay cap updoming are underlain by electrically more resistive zones (0.02-0.05 S/m), interpreted to be formed by propylitic alteration (Fig. 4 b). Since the magma reservoir C2 is situated beneath these alteration zones and the areas of clay cap updoming is the most obvious candidate for being the major heat source that drives hydrothermal convection within Aluto's geothermal system. The existence of an active magma reservoir below Aluto is also supported by increased emissions of volcanic gas along the Artu-Jawe-Fault Zone and occurrences of magma-derived fluids in hot springs and geothermal wells at Aluto (Gianelli & Teklemariam, 1993; Hochstein et al., 2017; Jolie et al., 2021; Regenspurg et al., 2022).

4 Discussion

The electrical conductivity structure, revealed by our 3-D multi-scale model, is in agreement with the concept and models of magma-assisted continental rifting (e.g. Beutel et al., 2010; Buck, 2004; Casey et al., 2006; Corti, 2009; Doubre et al., 2007; Kendall et al., 2005; T. O. Rooney et al., 2011; Rychert et al., 2012). A unique feature of our 3-D model is that it images, according to our interpretation, both the distribution of melt throughout the crust and the geothermal system below Aluto. Based on this model and previous studies, we present an updated conceptual model of the transcrustal structure across the CMER valley in the Aluto region in Fig. 7 and discuss it below.

4.1 Aluto's geothermal system

Hosting the only operating geothermal power plant in Ethiopia, the Aluto-Langano geothermal field was subject to several earlier local MT studies (Cherkose & Mizunaga, 2018; Samrock et al., 2015, 2020, 2023). The most recent study by Samrock et al. (2023) has shown, that the eastern area of clay cap updoming (Fig. 4 b) correlates with a hydrothermal upflow zone associated with a fault, in which all productive geothermal wells are drilled (e.g. Gianelli & Teklemariam, 1993; Hochstein et al., 2017). In agreement with Samrock et al. (2023) our model shows a second western zone of clay cap updoming (Fig. 4 b) that can be interpreted to be caused by hydrothermal upflow that is also spatially coherent with a fault. In this area no geothermal wells have been drilled yet, hence we propose this to be a potential area for future geothermal exploration drilling.

4.2 Architecture of the transcrustal magmatic system

Asthenospheric upwelling in the CMER is asymmetric with respect to the rift axis and focused to the western rift valley beneath the SDFZ as indicated by C3 (Fig. 5). The focusing of magmatic melt-ponding below the SDFZ is surprising, considering that the eastern rift valley is much more active in terms of volcano-tectonic activity along the WFB and eastern border faults (e.g. Corti et al., 2020; Keir et al., 2006; Mazzarini et al., 2013).

A plausible explanation for this asymmetry of asthenospheric upwelling can be an initial inhomogeneity in the lower crust. Areas with a local increase in thickness of the crust promote lithospheric thinning by replacing stronger lithospheric mantle with weak crustal material. Such zones of lithospheric thinning focus asthenospheric upwelling, subsequent decompression melting and rifting (e.g. Corti & Manetti, 2006; Dunbar & Sawyer, 1996). Such initial crustal inhomogeneities are likely to exist along the MER valley, as it developed within a suture zone of the Mozambique belt, which is a proterozoic continental collision zone (e.g. Fig. 4 in Corti, 2009; Keranen & Klemperer, 2008).

However, as magma is not preferentially rising vertically upwards below the SDFZ, where the lithosphere is thinnest, but is instead moving at an angle towards the eastern WFB (C2) (Fig. 5), it is likely that other structural controls play a role in the formation of the magmatic pathways. Two possible mechanisms causing transcrustal magmatic melt migration from the western to the eastern rift valley can be considered: (i) during the early stage of orthogonal rifting, when the extension is perpendicular to the rift axis (Bonini et

al., 1997), so that melt emplacement could have occurred by lateral squeezing and ascent in subvertical dykes (see Fig. 29 in Corti et al., 2003). Numerical modelling has shown that magma migrates subvertically upwards in areas, where gravitational unloading dominates over tectonic stretching forces, so that maximum stress is vertical, causing a stress-barrier that deflects ascending dykes (Maccaferri et al., 2014). An alternative or additional explanation for melt migration towards the eastern WFB is (ii) that the obliquity of the CMER (e.g. Agostini et al., 2011a) leads to a focusing of the extension in the en-échelon structure of the WFB (Corti, 2009, and references therein) and magma prefers to migrate upwards (Maccaferri et al., 2014) along the formed shear zones as shown in analogue modelling studies (e.g. Corti et al., 2003; Corti, 2008). In the MER it has been observed that magmatic segments mimick the en-échelon geometry (e.g. Casey et al., 2006; Ebinger & Casey, 2001; Kendall et al., 2005; Keranen et al., 2004).

The spatial correlation of the fault system at Aluto and the magma ascent channel (Fig. 5) is in agreement with the concept of "self-sustained" magmatic segments (e.g. Beutel et al., 2010; Corti, 2009; Kendall et al., 2005). Within this concept, magmatic intrusions weaken the lithosphere by intrusive heating and thus significantly lower the yield stress required to break up the lithosphere (e.g. van Wijk & Blackman, 2007; Buck, 2004; Hayward & Ebinger, 1996). Corti (2009) interpreted lithospheric weakening through intrusions to be responsible for strain localisation in magmatic segments of the MER. Numerical modelling by Beutel et al. (2010) further showed that cooled magmatic intrusions act as focal points for subsequent magmatic intrusions, explaining the recurrence of magmatic activity within the magmatic segments throughout many rifting episodes.

According to the interpretation of the presented conductivity anomalies (C3-C2: Fig. 5, 6), magma accumulates in the lower crust (C3), where high temperatures maintain melt-hosting regions, even if the magma concentration is low (e.g. Cashman et al., 2017). Segregated magma migrates upwards and is stored in a smaller upper crustal reservoir (C2 in Fig. 4 b), which represents only the small, uppermost part of the much larger, well-developed magma system (Mazzarini et al., 2013; T. O. Rooney et al., 2011). This interpretation of the transcrustal magma system is in agreement with recent concepts and subsurface models, where magma storage occurs in form of multiple interconnected magmatic mush systems and at different levels, rather than in isolated voluminous magma chambers (e.g. Cashman et al., 2017; Hill et al., 2022).

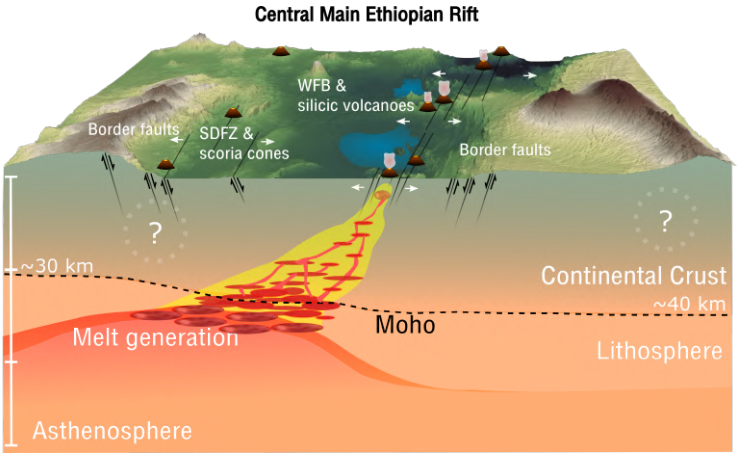

Figure 7. Conceptual model of the CMER. Asthenospheric upwelling leads to decompression melting. Buoyancy effects lead to upward migration of melt and melt ponding in the lower crust. Magma from the lower crustal ponding zone is fed into transcrustal magmatic mush systems that form along structural damage zones. The transcrustal magma system below the WFB is well developed. Here, magma rises quickly and fractionates in shallow magma reservoirs beneath silicic volcanoes, such as Aluto. The transcrustal magma system below the SDFZ is less mature and is not clearly imaged in this study. This might be caused by a lack of significant amounts of electrically conductive melt below the SDFZ, combined with a sparser MT site spacing in this area. Areas in the conceptual model that are less constrained by data are indicated by a question mark.

The shallow magmatic mush reservoir below Aluto is in a highly crystalline degassing state (Samrock et al., 2021) with a melt fraction of $\approx 10-15$ vol% and a magmatic volatile phase of ≥ 5 vol%. Hence, it can be considered to be non-eruptible, considering that for example Cashman et al. (2017, and references therein) define magma reservoirs as eruptable when melt fractions exceed 35 vol%. However, according to our interpretation, our model suggests that the shallow magmatic reservoir under Aluto could be recharged by magma transport from the lower crustal magma ponding zone (C3: maximum melt fraction 7 vol%) and through the magma channel C2. Admittedly, a detailed estimation of magma flux is not feasible within the scope of this study.

In contrast to the crustal structure below the WFB, our model does not show enhanced upper crustal electrical conductivities below the monogenetic vents in the western SDFZ region (Figs. 4,5,6). To make sure that the absence of a high electrical conductivity anomaly beneath the SDFZ cannot be attributed to a lack of data sensitivity, we perform a sensitivity test. The sensitivity test proves that with the given site distribution, the MT data would indeed be sensitive to an electrical conductor beneath the SDFZ, if it had a volume of $5 \times 5 \times 29\,\mathrm{km}^3$ comparable to the magma ascent channel C2 (SI: Text S6.). The absence of

a significant electrical conductivity anomaly under the SDFZ can be explained by the fact that ancient magma channels of the monogenetic vents are ephemeral and cooled quickly. If small amounts of melt are still present, melt is probably stored in the form of a highly crystalline and poorly interconnected mush and is therefore more difficult to image, given the rather sparse distribution ($4 - 13$ km) of MT stations in this region. This is supported by petrological studies, which suggest that melt rises in a complex dike system and is stored at multiple levels under the SDFZ, where it cools (e.g. Mazzarini et al., 2013; T. O. Rooney et al., 2011). The absence of significant amounts of melt in the upper crust under the SDFZ is also in agreement with the observed relatively low seismic activity beneath this area (Keir et al., 2006), which possibly hints at much fewer or no ongoing magma intrusions in that region. This relatively low seismic activity can be interpreted as a sign that the SDFZ accommodates only a subordinate fraction of strain in the CMER, which is consistent with a relatively weak surface expression of faults in the SDFZ compared to the WFB and border faults (e.g. Mazzarini et al., 2013; Agostini et al., 2011a). The lack of magmatic modification in combination with a relatively low extension activity in the SDFZ (Agostini et al., 2011a; Keir et al., 2006) support the concept that tectono-magmatic processes in the CMER maintain each other and that the lack of one leads to lower activity of the other (e.g. Beutel et al., 2010; Corti, 2009).

Despite the absence of significant electrical conductivity anomalies in the upper crust under the SDFZ, it is important to point out that past volcanic activity in the SDFZ most likely originated from the imaged deeper magmatic ponding zone (C3). Thus, our model suggests that magmas, erupted at the SDFZ and at Aluto within the WFB, may come from a common magma source, which would be the lower crustal magma ponding zone (C3) in our nomenclature. Although some geochemical studies have suggested spatially separated lower crustal melt ponding zones for the volcanoes located along the fault zones of the SDFZ and the WFB (e.g. T. O. Rooney et al., 2011), recent studies show that compositional variations can be explained solely by different rates of magma ascent, rather than by the existence of distinct melt reservoirs (Nicotra et al., 2021).

Our 3-D model differs in parts from the 2-D model by Hübert et al. (2018, Fig. 5), who performed a 2-D inversion of the 120 km long MT profile crossing Aluto (Fig. 1, see SI: Tab. 1). Hübert et al. (2018) imaged a strong electrical conductivity anomaly below the SDFZ, situated at much shallower depths than the lower magma ponding zone (C3) in our model. Furthermore, the 2-D model of Hübert et al. (2018) did not image a magma ascent

channel between the deeper source and Aluto volcano. There can be several reasons for the observed differences between the models. First, a large portion of the data exhibit 3-D effects, requiring a 3-D interpretation and hence 3-D inversion of the data (see SI: Fig. S4) and, indeed, we observe significant electrical conductivity variations along the rift (Fig. 6), which demand and justify a 3-D modelling approach. Second, in our new study we analyze substantially more MT stations, that are distributed in the western study area south and north of the profile line, than what was interpreted by Hübert et al. (2018). Furthermore, with 165 MT stations at Aluto, the density of MT sites in our study is significantly higher at the volcano, which can further contribute to the observed differences.

4.3 Conceptual model in the regional context of the MER

To complete the discussion, we put our conceptual model of the imaged segment in the CMER (Fig. 7) into the regional context of rifting in the MER.

Past regional-scale geoscientific studies along the central MER found evidence for tectono-magmatic processes that are also supported by our model. A low-velocity anomaly in seismic shear wave models is indicative of the presence of melt in the western lower crust (e.g. Kim et al., 2012). The low-velocity zone correlates with the area, where Stuart et al. (2006) inferred minimum Moho depths. Seismicity is focused in an area below the Wonji Fault Belt, which also hosts the silicic volcanoes including Aluto (e.g. Keir et al., 2006). Magma fractionates at shallow crustal levels below the WFB and at multiple levels below the SDFZ (T. O. Rooney et al., 2011). Our model supports these previous findings, which form the basis for the generalized conceptual model of the CMER proposed by i.a. T. O. Rooney et al. (2011). Hence, we propose that our new conceptual model might also describe the situation in other areas of the CMER and that it can be seen as a complementary model to current conceptual CMER models. The major difference in our new model is that it suggests that volcanoes along the WFB and the SDFZ likely share a common parental melt source below the SDFZ, that is imaged as conductor C3 (Fig. 5).

Furthermore, our study suggests, that the lateral distribution of melt in the lower crust along the rift valley is not uniform (Fig. 6). Electrical conductivities as high as in conductor C3 have not been imaged below the northernmost MT stations, but only in the southwestern survey area. This distribution of electrical conductivities in the lower crust indicates that melt fractions vary along the rift valley, which has not been resolved by the

existing regional seismic models (e.g. Chambers et al., 2022; Kim et al., 2012), to the best of our knowledge. To constrain this variation in more detail, additional MT soundings would be required further to the north and south of the survey area. However, we want to point out that also approximately 110 km north of our study area an MT study imaged high electrical conductivities west of the rift axis that were interpreted as magmatic melt at a depth of about 25 km (Whaler & Hautot, 2006).

The CMER is characterized to be in an asymmetric rifting stage, transitioning between rift initiation and incipient continental break-up (e.g. Agostini et al., 2011a). Our model is in agreement with the description of the CMER to be in this transitioning stage as it shows characteristic features of early and more mature rifting stages. As discussed earlier, asymmetric asthenospheric upwelling indicated by a focus of lower crustal magma ponding below the western part of the rift (C3: Fig. 5) can be interpreted as a remnant fingerprint of inherited crustal structures that influenced the first phases of rifting (e.g. Corti, 2009; Corti & Manetti, 2006; Courtillot, 1982; Dunbar & Sawyer, 1996; Keranen & Klemperer, 2008). The focused tectono-magmatic activity in the WFB (C2: Fig. 5) can be attributed to a more recent second phase rifting stage (e.g. Beutel et al., 2010; Bonini et al., 1997; Corti et al., 2003; Ebinger et al., 1987; van Wijk & Blackman, 2007).

The northern MER (NMER) is known to be in a more advanced stage of rifting than the CMER, characterized as incipient continental rupture (e.g. Agostini et al., 2011a; Keranen & Klemperer, 2008). As expected for an advanced rifting stage, the continental crust of the NMER is more symmetric across the rift and thinner than in the CMER (e.g. Stuart et al., 2006; Agostini et al., 2011a). Furthermore, in the NMER strain is focused in the en-échelon segments (Corti et al., 2018). Hence, the magma-tectonic setting in the NMER suggests that here, lower crustal melt ponding is rift-axis centered beneath the WFB and not asymmetric as observed in the CMER. However, a systematic comparison of transcrustal structures throughout the different rifting stages of the MER is difficult, since models of the transcrustal magmatic melt distribution, that are comparable to this study are lacking for the northern MER. Existing models of rift-wide shear wave velocities of the CMER and the NMER are not detailed enough to map differences of the cross-rift magma distribution at $20 - 40$ km depth (Fig. 8 in Chambers et al., 2022).

4.4 A global perspective on transcrustal magmatic systems

In the context of different tectonic systems worldwide, magmatic underplating and ponding in stacked sills at the base of the crust, as is suggested by our model (C3), is a widely adopted concept, but detailed imaging of such zones has been rare (e.g. Cashman et al., 2017; Thybo & Artemieva, 2013). However, there is an increasing number of geophysical MT studies that image such vertically extensive trans-crustal magmatic systems (Bedrosian et al., 2018; Comeau et al., 2016, 2021; Hill et al., 2009, 2022; Käufl et al., 2020; Wannamaker et al., 2008).

A direct comparison of our model from the CMER with the magmatic system of the volcano Mt. Erebus in the Terror Rift of Antarctica, imaged by MT, reveals similar interdependencies of tectono-magmatic processes. At Mt. Erebus the transcrustal magma distribution has a vertically oblique geometry and lower crustal melt fractions of 10 vol% (Hill et al., 2022), both features that are comparable to the CMER, as imaged by us with an estimated lower crustal melt fraction of 7 vol%. However, Oppenheimer et al. (2011) suggest that CO_2 streaming dehydrates magma at Mt. Erebus and the resulting low water content (H_2O:$\sim$ 0.1 wt%) allows magma storage at very shallow depths ($\leq$ 1 km) below Mt. Erebus (Hill et al., 2022), which is apparently not the case for Aluto, where the dissolved volatile fraction in the melt is larger (C2: $\geq$ 4 km, H_2O:$\sim$ 4.7 wt% from Samrock et al. (2021)).

The significance of the interplay between mantle dynamics and stress and strain distribution within the crust, which controls transcrustal magma distribution, has been highlighted by studies, conducted in different tectonic settings, which we briefly outline in the following. On a global scale, processes initiating magma supply can be categorized to be either (i) bottom-up controlled through active mantle upwelling and the influence of hot buoyant mantle plumes or (ii) top-down controlled through tectonic processes initiating convection and thus passive magma upwelling (e.g. Li et al., 2022). However, on a local scale either magmatic or tectonic processes might exercise greater control on the lithosphere. In a convergent intraplate setting, induced asthenospheric upwelling and subsequent passive magmatism dominate the crustal structure by initiating topographic uplift and volcanism (Comeau et al., 2021; Käufl et al., 2020). In contrast, in subduction systems, it has been shown that inhomogeneities in the crust, such as boundaries between lithological units focus magmatism (Bedrosian et al., 2018; Comeau et al., 2016; Hill et al., 2009). On the other

hand,in a ceasing active rifting regime no dominant control could be identified (Wannamaker et al., 2008).

The CMER, as imaged in this study, is a good example for a system in which both bottom-up and top-down processes did control rifting in the past. It is commonly assumed that rifting in the MER initiated under the influence of a magma plume (Corti, 2009; Courtillot et al., 1999) (bottom-up control), whereas later asthenospheric upwelling might have been controlled by crustal inhomogeneities (top-down control) (Corti & Manetti, 2006). Today, rifting appears to be driven by self-sustaining tectono-magmatic systems, such as the Wonji Fault Belt, where magma supply and strain focusing enforce each other (Beutel et al., 2010; Buck, 2004; Corti, 2009; Hayward & Ebinger, 1996; Kendall et al., 2005; van Wijk & Blackman, 2007).

5 Conclusions and Outlook

Our model provides a 3-D subsurface image of the electrical conductivity distribution in the Aluto volcano region within the Main Ethiopian Rift. The model provides new insights into regional geological structures across the rift and the local geothermal system under Aluto. The major contributions of this study are: (i) imaging the electrical conductivity structure of the lower crustal magma ponding zone and imposing bounds on its lateral extent and thermo-chemical state (ii) as well as imaging the magmatic and hydrothermal systems under Aluto and their connection to the deep-seated lower crustal magma source.

The number of geophysical models imaging transcrustal magmatic mush systems at this scale (e.g. Cashman et al., 2017) is still limited (e.g. Bedrosian et al., 2018; Comeau et al., 2016, 2021; Hill et al., 2009; Huang et al., 2015; Käufl et al., 2020), especially in the setting of active continental rifts (e.g. Hill et al., 2022; Wannamaker et al., 2008). Our study (Fig. 7) provides previously missing geophysical evidence for the hypothesized conceptual model of the Central Main Ethiopian Rift (e.g. T. O. Rooney et al., 2011). The results are in agreement with the conceptual understanding of the Central Main Ethiopian Rift, where asthenospheric upwelling beneath the western rift valley leads to decompression melting, feeding magma towards the subordinate western and more mature eastern tectono-magmatic segments of the Wonji Fault Belt. The crust below the en-échelon fault systems of the Wonji Fault Belt hosts transcrustal magmatic melt systems, which provide the heat

that drives prospective geothermal systems, that are found within the magmatic segments of the Wonji Fault Belt.

These observations, and the subsequent geological interpretation, were enabled by combining regional and local magnetotelluric datasets and by using a modern multi-scale magnetotelluric imaging approach. Future regional-scale MT studies along the rift valley are required to provide further insights into along-rift variations of the lower crustal magma ponding zone (C3) and its connection to the other two major volcanic geothermal centers. Two other major volcanoes are Tulu Moye and Corbetti, located north and south of Aluto respectively, where high-resolution MT surveys, comparable to the one at Aluto, have been conducted (Gíslason et al., 2015; Samrock et al., 2018). One avenue for potential future research will be further work on volcanic risk assessment and geothermal exploration. Both applications would benefit from further quantitative analyses of transcrustal magmatic melt fractions, constrained by electrical conductivity subsurface models. As such, electrical conductivity can be used to better constrain quantitative characteristics of magmatic systems and to estimate magmatic fluxes (e.g. M. L. M. Gleeson et al., 2023) and the formation of convective hydrothermal system above magmatic intrusions (e.g. Scott, 2020).

Data availability

The MT data collected at Aluto by ETH Zurich are available from Samrock et al. (2010) via the IRIS EMTF Database: `http://ds.iris.edu/spud/emtf` under the Project entry "Ethiopia", and the survey name "Aluto-Langano Geothermal" (Project ID Ethiopia.R1.2012). The MT-dataset by project RiftVolc from Hübert and Whaler (2020) is available under the DOI: `https://doi.org/10.5285/2fb02ed4-5f50-4c14-aeec-27ee13aafc38`. The MT data by the Geological Survey of Ethiopia are available for academic purposes on request from the Geological Survey of Ethiopia (`www.mom.gov.et`), as was the case for this study. The model is available for download in the ETH research collection (`www.research-collection.ethz.ch`) under Dambly et al. (2022) (DOI: `https://doi.org/10.3929/ethz-b-000576313`) in form of a Visualization Toolkit (VTK) data file for ParaView.

Declaration of competing interest

The authors declare that they have no known competing financial interests or personal relationships that could have appeared to influence the work reported in this paper.

CReDit Authorship statement

M.L.T.D. performed modelling and inversion of the magnetotelluric data, model visualization and developed numerical tools. F.S. contributed to the 3-D modelling and inversion of the data and model visualization. A.G. developed the GoFEM code and contributed to the 3-D modelling and inversion of the data. All authors interpreted the results and contributed to the writing and review of the paper.

Acknowledgments

M.L.T.D. was supported by ETH Grant ETH-02 19-1. A.G. was supported by the Heisenberg Grant from the German Research Foundation, Deutsche Forschungsgemeinschaft (Project No. 465486300). 3-D inversions and modelling were carried out at the Swiss National Supercomputing Center (CSCS) under project ID s1106. We thank Juliane Hübert and Kathy Whaler from Project RiftVolc and the Geological Survey of Ethiopia for making MT data available. We acknowledge the use of MTPy (Kirkby et al., 2019; Krieger & Peacock, 2014), Generic Mapping Tools (GMT), and Paraview, and thank NASA for providing SRTM digital elevation models. M.O.S., F.S. and M.L.T.D. thank the Werner Siemens Foundation (Werner Siemens-Stiftung) for their endowment of the Geothermal Energy and Geofluids (GEG.ethz.ch) group at ETH Zurich.

References

Agostini, A., Bonini, M., Corti, G., Sani, F., & Manetti, P. (2011a). Distribution of quaternary deformation in the central Main Ethiopian Rift, East Africa. *Tectonics*, *30*(4), 1–21. doi: 10.1029/2010TC002833

Agostini, A., Bonini, M., Corti, G., Sani, F., & Manetti, P. (2011b). *Distribution of quaternary deformation in the central Main Ethiopian Rift, East Africa* [dataset]. (Access Fault Dataset 2.5 `http://ethiopianrift.igg.cnr.it/utilities.htm`) doi: 10.1029/2010TC002833

Árnason, K., Karlsdóttir, R., Eysteinsson, H., Flóvenz, Ó. G., & Gudlaugsson, S. T. (2000). The resistivity structure of high-temperature geothermal systems in Iceland. In *Proceedings of the world geothermal congress 2000* (pp. 923–928). Kyushu-Tohoku, Japan.

Arndt, D., Bangerth, W., Blais, B., Clevenger, T. C., Fehling, M., Grayver, A. V., ... Wells, D. (2020). The deal. II library, version 9.2. *Journal of Numerical Mathematics*, *28*(3), 131–146. doi: 10.1515/jnma-2020-0043

Ayalew, D., Jung, S., Romer, R. L., Kersten, F., Pfänder, J. A., & Garbe-Schönberg, D. (2016). Petrogenesis and origin of modern Ethiopian Rift basalts: Constraints from isotope and trace element geochemistry. *Lithos*, *258-259*, 1–14. doi: 10.1016/j.lithos.2016.04.001

Barberi, F., & Varet, J. (1978). The Afar rift junction. In *Petrology and Geochemistry of Continental Rifts: Volume One of the Proceedings of the NATO Advanced Study Institute Paleorift Systems with Emphasis on the Permian Oslo Rift, held in Oslo, Norway, July 27–August 5, 1977* (pp. 55–69). doi: 10.1007/978-94-009-9803-2

Bedrosian, P. A., Peacock, J. R., Bowles-Martinez, E., Schultz, A., & Hill, G. J. (2018). Crustal inheritance and a top-down control on arc magmatism at Mount St Helens. *Nature Geoscience*, *11*(11), 865–870. doi: 10.1038/s41561-018-0217-2

Benti, N. E., Woldegiyorgis, T. A., Geffe, C. A., Gurmesa, G. S., Chaka, M. D., & Mekonnen, Y. S. (2023). Overview of geothermal resources utilization in Ethiopia: Potentials, opportunities, and challenges. *Scientific African*, e01562. doi: 10.1016/j.sciaf.2023.e01562

Berdichevsky, M. N., & Dmitriev, V. I. (2008). *Models and methods of magnetotellurics*. Springer, Berlin. doi: 10.1007/978-3-540-77814-1

Bertrand, E. A., Caldwell, T. G., Hill, G. J., Wallin, E. L., Bennie, S. L., Cozens, N., ... Wameyo, P. (2012). Magnetotelluric imaging of upper-crustal convection plumes beneath the Taupo Volcanic Zone, New Zealand. *Geophysical Research Letters*, *39*(2). doi: 10.1029/2011GL050177

Beutel, E., van Wijk, J., Ebinger, C., Keir, D., & Agostini, A. (2010). Formation and stability of magmatic segments in the Main Ethiopian and Afar Rifts. *Earth and Planetary Science Letters*, *293*(3-4), 225–235. doi: 10.1016/j.epsl.2010.02.006

Biggs, J., Ayele, A., Fischer, T. P., Fontijn, K., Hutchison, W., Kazimoto, E., ... Wright, T. J. (2021). Volcanic activity and hazard in the East African Rift zone. *Nature Communications*, *12*(1), 1–12. doi: 10.1038/s41467-021-27166-y

Bonini, M., Corti, G., Innocenti, F., Manetti, P., Mazzarini, F., Abebe, T., & Pecskay, Z. (2005, 02). Evolution of the Main Ethiopian Rift in the frame of Afar and Kenya rifts propagation. *Tectonics*, *24*(1). doi: 10.1029/2004TC001680

Bonini, M., Souriot, T., Boccaletti, M., & Brun, J. P. (1997). Successive orthogonal and oblique extension episodes in a rift zone: Laboratory experiments with application to the Ethiopian Rift. *Tectonics*, *16*(2), 347-362. doi: 10.1029/96TC03935

Booker, J. R. (2014). The magnetotelluric phase tensor: a critical review. *Surveys in Geophysics*, *35*(1), 7–40. doi: 10.1007/s10712-013-9234-2

Brune, S., Kolawole, F., Olive, J.-A., Stamps, D. S., Buck, W. R., Buiter, S. J., ... Shillington, D. J. (2023). Geodynamics of continental rift initiation and evolution. *Nature Reviews Earth & Environment*, 1–19. doi: 10.1038/s43017-023-00391-3

Buck, W. R. (2004). Consequences of asthenospheric variability on continental rifting. In G. D. Karner, B. Taylor, N. W. Driscoll, & D. L. Kohlstedt (Eds.), *Rheology and deformation of the lithosphere at continental margins* (pp. 1–30). New York: Columbia University Press. doi: 10.7312/karn12738-002

Burnside, N., Montcoudiol, N., Becker, K., & Lewi, E. (2021). Geothermal energy resources in Ethiopia: Status review and insights from hydrochemistry of surface and groundwaters. *Wiley Interdisciplinary Reviews: Water*, e1554. doi: 10.1002/wat2.1554

Caldwell, T. G., Bibby, H. M., & Brown, C. (2004). The magnetotelluric phase tensor. *Geophysical Journal International*, *158*(2), 457–469. doi: 10.1111/j.1365-246X.2004.02281.x

capitalethiopia.com. (2022). *Production tests kick start at Aluto Langano.* Retrieved from `https://www.capitalethiopia.com/capital/production-tests-kick-start-at-aluto-langano/` (accessed 14 October 2022)

Casey, M., Ebinger, C. J., Keir, D., Gloaguen, R., & Mohamed, F. (2006). Strain accommodation in transitional rifts: Extension by magma intrusion and faulting in Ethiopian rift magmatic segments. *Environmental Geochemistry and Health, With Special Reference to Developing Countries*, *259*(2003), 143–163. doi: 10.1144/GSL.SP.2006.259.01.13

Cashman, K. V., Sparks, R. S. J., & Blundy, J. D. (2017). Vertically extensive and unstable magmatic systems: A unified view of igneous processes. *Science*, *355*(6331). doi: 10.1126/science.aag3055

Cawthorn, R. G., & Walraven, F. (1998, 09). Emplacement and Crystallization Time for the Bushveld Complex. *Journal of Petrology*, *39*(9), 1669-1687. doi: 10.1093/petroj/39.9.1669

Chambers, E. L., Harmon, N., Keir, D., & Rychert, C. A. (2019). Using ambient noise to image the northern East African Rift. *Geochemistry, Geophysics, Geosystems*, *20*(4), 2091–2109. doi: 10.1029/2018GC008129

Chambers, E. L., Harmon, N., Rychert, C. A., Gallacher, R. J., & Keir, D. (2022, 04).

Imaging the seismic velocity structure of the crust and upper mantle in the northern East African Rift using rayleigh wave tomography. *Geophysical Journal International*. doi: 10.1093/gji/ggac156

Chave, A. D., & Jones, A. G. (2012). *The magnetotelluric method: Theory and practice*. Cambridge University Press, New York. doi: 10.1017/CBO9781139020138

Cherkose, B. A., & Mizunaga, H. (2018). Resistivity imaging of Aluto-Langano geothermal field using 3-D magnetotelluric inversion. *Journal of African Earth Sciences*, *139*, 307-318. doi: 10.1016/j.jafrearsci.2017.12.017

Colombier, M., Wadsworth, F. B., Gurioli, L., Scheu, B., Kueppers, U., Di Muro, A., & Dingwell, D. B. (2017, March). The evolution of pore connectivity in volcanic rocks. *Earth and Planetary Science Letters*, *462*(15), 99–109. doi: 10.1016/j.epsl.2017.01.011

Comeau, M. J., Stein, C., Becken, M., & Hansen, U. (2021). Geodynamic modeling of lithospheric removal and surface deformation: Application to intraplate uplift in Central Mongolia. *Journal of Geophysical Research: Solid Earth*, *126*(5), e2020JB021304. doi: 10.1029/2020JB021304

Comeau, M. J., Unsworth, M. J., & Cordell, D. (2016, 10). New constraints on the magma distribution and composition beneath Volcán Uturuncu and the southern Bolivian Altiplano from magnetotelluric data. *Geosphere*, *12*(5), 1391-1421. doi: 10.1130/GES01277.1

Corti, G. (2008). Control of rift obliquity on the evolution and segmentation of the main Ethiopian rift. *Nature Geoscience*, *1*(4), 258–262. doi: 10.1038/ngeo160

Corti, G. (2009). Continental rift evolution: From rift initiation to incipient break-up in the Main Ethiopian Rift, East Africa. *Earth-Science Reviews*, *96*(1-2), 1–53. doi: 10.1016/j.earscirev.2009.06.005

Corti, G., Bonini, M., Conticelli, S., Innocenti, F., Manetti, P., & Sokoutis, D. (2003). Analogue modelling of continental extension: A review focused on the relations between the patterns of deformation and the presence of magma. *Earth-Science Reviews*, *63*(3-4), 169–247. doi: 10.1016/S0012-8252(03)00035-7

Corti, G., & Manetti, P. (2006). Asymmetric rifts due to asymmetric mohos: An experimental approach. *Earth and Planetary Science Letters*, *245*(1), 315-329. doi: 10.1016/j.epsl.2006.02.004

Corti, G., Molin, P., Sembroni, A., Bastow, I. D., & Keir, D. (2018). Control of pre-rift

lithospheric structure on the architecture and evolution of continental rifts: Insights from the Main Ethiopian Rift, East Africa. *Tectonics*, *37*(2), 477-496. doi: 10.1002/2017TC004799

Corti, G., Sani, F., Florio, A. A., Greenfield, T., Keir, D., Erbello, A., ... Ayele, A. (2020). Tectonics of the Asela-Langano margin, Main Ethiopian Rift (East Africa). *Tectonics*, *39*(8), e2020TC006075. doi: 10.1029/2020TC006075

Courtillot, V. (1982). Propagating rifts and continental breakup. *Tectonics*, *1*(3), 239-250. doi: 10.1029/TC001i003p00239

Courtillot, V., Jaupart, C., Manighetti, I., Tapponnier, P., & Besse, J. (1999). On causal links between flood basalts and continental breakup. *Earth and Planetary Science Letters*, *166*(3), 177-195. doi: 10.1016/S0012-821X(98)00282-9

Dai, L., Hu, H., Li, H., Hui, K., Jiang, J., Li, J., & Sun, W. (2015, 03). Electrical conductivity of gabbro: the effects of temperature, pressure and oxygen fugacity. *European Journal of Mineralogy*, *27*(2), 215-224. doi: 10.1127/ejm/2015/0027-2429

Dambly, M. L. T., Samrock, F., Grayver, A., & Saar, M. O. (2022). *Transcrustal 3-D electrical conductivity model of the Central Main Ethiopian Rift* [Model]. doi: 10.3929/ethz-b-000576313

Desissa, M., Johnson, N. E., Whaler, K. A., Hautot, S., Fisseha, S., & Dawes, G. J. (2013). A mantle magma reservoir beneath an incipient mid-ocean ridge in Afar, Ethiopia. *Nature Geoscience*, *6*(10), 861–865. doi: 10.1038/ngeo1925

Doubre, C., Manighetti, I., Dorbath, L., Dorbath, C., Bertil, D., & Delmond, J. C. (2007). Crustal structure and magmato-tectonic processes in an active rift (Asal-Ghoubbet, Afar, East Africa): 2. Insights from the 23-year recording of seismicity since the last rifting event. *Journal of Geophysical Research: Solid Earth*, *112*(B5). doi: 10.1029/2006JB004333

Dunbar, J. A., & Sawyer, D. S. (1996). Three-dimensional dynamical model of continental rift propagation and margin plateau formation. *Journal of Geophysical Research: Solid Earth*, *101*(B12), 27845-27863. doi: 10.1029/96JB01231

Ebinger, C. (2005, 04). Continental break-up: The East African perspective. *Astronomy & Geophysics*, *46*(2), 2.16-2.21. doi: 10.1111/j.1468-4004.2005.46216.x

Ebinger, C., & Casey, M. (2001, 06). Continental breakup in magmatic provinces: An Ethiopian example. *Geology*, *29*(6), 527-530. doi: 10.1130/0091-7613(2001)029⟨0527:CBIMPA⟩2.0.CO;2

Ebinger, C., Rosendahl, B., & Reynolds, D. (1987). Tectonic model of the Malawi rift, Africa. *Tectonophysics*, *141*(1), 215-235. doi: 10.1016/0040-1951(87)90187-9

Field, L., Blundy, J., Calvert, A., & Yirgu, G. (2013, January). Magmatic history of Dabbahu, a composite volcano in the Afar Rift, Ethiopia. *Bulletin*, *125*(1-2), 128–147. doi: 10.1130/B30560.1

Flóvenz, Ó., Hersir, G., Sæmundsson, K., Ármannsson, H., & Fridriksson, P. (2012). 7.03 - geothermal energy exploration techniques. In A. Sayigh (Ed.), *Comprehensive renewable energy* (p. 51-95). Oxford: Elsevier. doi: 10.1016/B978-0-08-087872-0.00705-8

Fontijn, K., McNamara, K., Tadesse, A. Z., Pyle, D. M., Dessalegn, F., Hutchison, W., ... Yirgu, G. (2018). Contrasting styles of post-caldera volcanism along the Main Ethiopian Rift: Implications for contemporary volcanic hazards. *Journal of Volcanology and Geothermal Research*, *356*, 90–113. doi: 10.1016/j.jvolgeores.2018.02.001

Fritzsche, F., Zech, W., & Guggenberger, G. (2007). Soils of the Main Ethiopian Rift valley escarpment: A transect study. *CATENA*, *70*(2), 209-219. doi: 10.1016/j.catena.2006.09.005

Gallacher, R. J., Keir, D., Harmon, N., Stuart, G., Leroy, S., Hammond, J. O., ... Ahmed, A. (2016). The initiation of segmented buoyancy-driven melting during continental breakup. *Nature Communications*, *7*, 1–9. doi: 10.1038/ncomms13110

Geshi, N., Ruch, J., & Acocella, V. (2014). Evaluating volumes for magma chambers and magma withdrawn for caldera collapse. *Earth and Planetary Science Letters*, *396*, 107-115. doi: 10.1016/j.epsl.2014.03.059

Geyer, A., Folch, A., & Martí, J. (2006). Relationship between caldera collapse and magma chamber withdrawal: An experimental approach. *Journal of Volcanology and Geothermal Research*, *157*(4), 375-386. doi: 10.1016/j.jvolgeores.2006.05.001

Ghiglieri, G., Pistis, M., Abebe, B., Azagegn, T., Asresahagne Engidasew, T., Pittalis, D., ... Haile, T. (2020). Three-dimensional hydrostratigraphical modelling supporting the evaluation of fluoride enrichment in groundwater: Lakes basin (Central Ethiopia). *Journal of Hydrology: Regional Studies*, *32*, 100756. doi: 10.1016/j.ejrh.2020.100756

Ghiorso, M. S., & Gualda, G. A. (2015). An H_2O–CO_2 mixed fluid saturation model compatible with rhyolite-MELTS. *Contributions to Mineralogy and Petrology*, *169*(6), 1–30. doi: 10.1007/s00410-015-1141-8

Gianelli, G., & Teklemariam, M. (1993). Water-rock interaction processes in the Aluto-Langano geothermal field (Ethiopia). *Journal of Volcanology and Geothermal Re-*

search, *56*(4), 429-445. doi: 10.1016/0377-0273(93)90007-E

Gíslason, G., Eysteinsson, H., Björnsson, G., & Hardardóttir, V. (2015). Results of surface exploration in the Corbetti geothermal area, Ethiopia. In *Proceedings world geothermal congress.* Melbourne, Australia.

Gleeson, M. L., Stock, M. J., Pyle, D. M., Mather, T. A., Hutchison, W., Yirgu, G., & Wade, J. (2017). Constraining magma storage conditions at a restless volcano in the Main Ethiopian Rift using phase equilibria models. *Journal of Volcanology and Geothermal Research*, *337*, 44–61. doi: 10.1016/j.jvolgeores.2017.02.026

Gleeson, M. L. M., Lissenberg, C. J., & Antoshechkina, P. (2023). Porosity evolution of mafic crystal mush during reactive flow. *Nature Communications*, *14*(3088). doi: 10.1038/s41467-023-38136-x

Glover, P. (2009, January). What is the cementation exponent? A new interpretation. *The Leading Edge*, *28*(1), 82–85. doi: 10.1190/1.3064150

Glover, P. (2015, 04). Geophysical properties of the near surface Earth: Electrical properties. In G. Schubert (Ed.), *Treatise on geophysics* (Second ed., pp. 89–137). Elsevier Oxford. doi: 10.1016/B978-0-444-53802-4.00189-5

Glover, P., Hole, M., & Pous, J. (2000, August). A modified Archie's law for two conducting phases. *Earth and Planetary Science Letters*, *180*(3-4), 369-383. doi: 10.1016/S0012-821X(00)00168-0

Grayver, A., Tietze, K., & Ritter, O. (2013, September). RMS-Rather Meaningless Simplification? In *Proceedings on the 25th schmucker-weidelt-kolloquium für elektromagnetische tiefenforschung* (pp. 31–35). Kirchhundem Rahrbach, Germany.

Grayver, A. V. (2015). Parallel three-dimensional magnetotelluric inversion using adaptive finite-element method. part i: Theory and synthetic study. *Geophysical Journal International*, *202*(1), 584–603. doi: 10.1093/gji/ggv165

Grayver, A. V., & Kolev, T. V. (2015). Large-scale 3D geoelectromagnetic modeling using parallel adaptive high-order finite element method. *Geophysics*, *80*(6), E277–E291. doi: 10.1190/geo2015-0013.1

Hammond, J. O., & Kendall, J. M. (2016). Constraints on melt distribution from seismology: A case study in Ethiopia. *Environmental Geochemistry and Health, With Special Reference to Developing Countries*, *420*(1), 127–147. doi: 10.1144/SP420.14

Hammond, W. C., & Humphreys, E. D. (2000, May). Upper mantle seismic wave attenuation: Effects of realistic partial melt distribution. *Journal of Geophysical Research,*

Solid Earth, *105*(B5), 10987–10999. doi: 10.1029/2000JB900042

Hashin, Z., & Shtrikman, S. (1962). A variational approach to the theory of the elastic behaviour of polycrystals. *Journal of the Mechanics and Physics of Solids*, *10*(4), 343–352. doi: 10.1016/0022-5096(62)90005-4

Hayward, N. J., & Ebinger, C. J. (1996). Variations in the along-axis segmentation of the Afar Rift system. *Tectonics*, *15*(2), 244-257. doi: 10.1029/95TC02292

Hill, G. J., Caldwell, T. G., Heise, W., Chertkoff, D. G., Bibby, H. M., Burgess, M. K., ... Cas, R. A. (2009). Distribution of melt beneath Mount St Helens and Mount Adams inferred from magnetotelluric data. *Nature Geoscience*, *2*(11), 785–789. doi: 10.1038/ngeo661

Hill, G. J., Wannamaker, P. E., Maris, V., Stodt, J. A., Kordy, M., Unsworth, M. J., ... Kyle, P. (2022). Trans-crustal structural control of CO_2-rich extensional magmatic systems revealed at Mount Erebus Antarctica. *Nature Communications*, *13*(1), 1–10. doi: 10.1038/s41467-022-30627-7

Hochstein, M. P., Oluma, B., & Hole, H. (2017). Early exploration of the Aluto geothermal field, Ethiopia (History of discovery well LA-3). *Geothermics*, *66*, 73-84. doi: 10.1016/j.geothermics.2016.11.010

Huang, H.-H., Lin, F.-C., Schmandt, B., Farrell, J., Smith, R. B., & Tsai, V. C. (2015). The Yellowstone magmatic system from the mantle plume to the upper crust. *Science*, *348*(6236), 773–776. doi: 10.1126/science.aaa5648

Hübert, J., & Whaler, K. (2020). *Magnetotelluric and transient electromagnetic data from the Main Ethiopian Rift. British Geological Survey. (dataset).* [dataset]. doi: 10.5285/2fb02ed4-5f50-4c14-aeec-27ee13aafc38

Hübert, J., Whaler, K., & Fisseha, S. (2018). The electrical structure of the central Main Ethiopian Rift as imaged by magnetotellurics: Implications for magma storage and pathways. *Journal of Geophysical Research, Solid Earth*, *123*(7), 6019–6032. doi: 10.1029/2017JB015160

Hunt, J. A., Mather, T. A., & Pyle, D. M. (2020). Morphological comparison of distributed volcanic fields in the Main Ethiopian Rift using high-resolution digital elevation models. *Journal of Volcanology and Geothermal Research*, *393*, 106732. doi: 10.1016/j.jvolgeores.2019.106732

Hunt, J. A., Zafu, A., Mather, T. A., Pyle, D. M., & Barry, P. H. (2017). Spatially variable CO_2 degassing in the Main Ethiopian Rift: Implications for magma storage, volatile

transport, and rift-related emissions. *Geochemistry, Geophysics, Geosystems*, *18*(10), 3714-3737. doi: 10.1002/2017GC006975

Hutchison, W., Biggs, J., Mather, T. A., Pyle, D. M., Lewi, E., Yirgu, G., ... Fischer, T. P. (2016). Causes of unrest at silicic calderas in the East African Rift: New constraints from InSAR and soil-gas chemistry at Aluto volcano, Ethiopia. *Geochemistry, Geophysics, Geosystems*, *17*(8), 3008–3030. doi: 10.1002/2016GC006395

Iddon, F., & Edmonds, M. (2020). Volatile-rich magmas distributed through the upper crust in the Main Ethiopian Rift. *Geochemistry, Geophysics, Geosystems*, *21*(6). doi: 10.1029/2019GC008904

IRENA. (2020). *Geothermal development in Eastern Africa: Recommendations for power and direct use*. Abu Dhabi: International Renewable Energy Agency.

Jolie, E., Scott, S., Faulds, J., Chambefort, I., Axelsson, G., Gutiérrez-Negrín, L. C., ... Zemedkun, M. T. (2021). Geological controls on geothermal resources for power generation. *Nature Reviews Earth & Environment*, *2*(5), 324–339. doi: 10.1038/s43017-021-00154-y

Kalscheuer, T., Pedersen, L. B., & Siripunvaraporn, W. (2008, November). Radiomagnetotelluric two-dimensional forward and inverse modelling accounting for displacement currents. *Geophysical Journal International*, *175*(2), 486–514. doi: 10.1111/j.1365-246X.2008.03902.x

Käufl, J. S., Grayver, A. V., Comeau, M. J., Kuvshinov, A. V., Becken, M., Kamm, J., ... Demberel, S. (2020). Magnetotelluric multiscale 3-D inversion reveals crustal and upper mantle structure beneath the Hangai and Gobi-Altai region in Mongolia. *Geophysical Journal International*, *221*(2), 1002–1028. doi: 10.1093/gji/ggaa039

Käufl, J. S., Grayver, A. V., & Kuvshinov, A. V. (2018). Topographic distortions of magnetotelluric transfer functions: A high-resolution 3-D modelling study using real elevation data. *Geophysical Journal International*, *215*(3), 1943–1961. doi: 10.1093/gji/ggy375

Keir, D., Ebinger, C. J., Stuart, G. W., Daly, E., & Ayele, A. (2006). Strain accommodation by magmatism and faulting as rifting proceeds to breakup: Seismicity of the northern Ethiopian Rift. *Journal of Geophysical Research, Solid Earth*, *111*(5), 1–17. doi: 10.1029/2005JB003748

Kelbert, A., Meqbel, N., Egbert, G. D., & Tandon, K. (2014, May). ModEM: A modular system for inversion of electromagnetic geophysical data. *Computers & Geosciences*,

66, 40–53. doi: 10.1016/j.cageo.2014.01.010

Kendall, J.-M., & Lithgow-Bertelloni, C. (2016). Why is Africa rifting? *Environmental Geochemistry and Health, With Special Reference to Developing Countries*, *420*(1), 11–30. doi: 10.1144/SP420.17

Kendall, J.-M., Stuart, G., Ebinger, C., Bastow, I., & Keir, D. (2005, 01). Magma-assisted rifting in Ethiopia. *Nature*, *433*(7022), 146–148. doi: 10.1038/nature03161

Keranen, K., Klemperer, S., Gloaguen, R., & Group, E. W. (2004, 11). Three-dimensional seismic imaging of a protoridge axis in the Main Ethiopian rift. *Geology*, *32*(11), 949-952. Retrieved from `10.1130/G20737.1` doi: 10.1130/G20737.1

Keranen, K., & Klemperer, S. L. (2008). Discontinuous and diachronous evolution of the Main Ethiopian Rift: Implications for development of continental rifts. *Earth and Planetary Science Letters*, *265*(1-2), 96–111. doi: 10.1016/j.epsl.2007.09.038

Kim, S., Nyblade, A. A., Rhie, J., Baag, C. E., & Kang, T. S. (2012). Crustal S-wave velocity structure of the Main Ethiopian Rift from ambient noise tomography. *Geophysical Journal International*, *191*(2), 865–878. doi: 10.1111/j.1365-246X.2012.05664.x

King, G., & Bailey, G. (2006). Tectonics and human evolution. *Antiquity*, *80*(308), 265–286. doi: 10.1017/S0003598X00093613

Kirkby, A. L., Zhang, F., Peacock, J., Hassan, R., & Duan, J. (2019). The MTPy software package for magnetotelluric data analysis and visualisation. *Journal of Open Source Software*, *4*(37), 1358. doi: 10.21105/joss.01358

Krieger, L., & Peacock, J. R. (2014). MTpy: A python toolbox for magnetotellurics. *Computers & Geosciences*, *72*, 167-175. doi: 10.1016/j.cageo.2014.07.013

Kristmannsdottir, H. (1979). Alteration of basaltic rocks by hydrothermal-activity at 100-300°C. In M. Mortland & V. Farmer (Eds.), *International clay conference 1978* (Vol. 27, p. 359-367). Elsevier. doi: 10.1016/S0070-4571(08)70732-5

Lévy, L., Gibert, B., Sigmundsson, F., Flóvenz, Ó., Hersir, G. P., Briole, P., & Pezard, P. A. (2018). The role of smectites in the electrical conductivity of active hydrothermal systems: Electrical properties of core samples from Krafla volcano, Iceland. *Geophysical Journal International*, *215*(3), 1558–1582. doi: 10.1093/gji/ggy342

Li, S., Li, X., Zhou, J., Cao, H., Liu, L., Liu, Y., ... Jiang, Z. (2022). Passive magmatism on Earth and Earth-like planets. *Geosystems and Geoenvironment*, *1*(1), 100008. doi: 10.1016/j.geogeo.2021.10.003

Maccaferri, F., Rivalta, E., Keir, D., & Acocella, V. (2014). Off-rift volcanism in rift zones

determined by crustal unloading. *Nature Geoscience*, *7*(4), 297–300. doi: 10.1038/ngeo2110

Mackenzie, G. D., Thybo, H., & Maguire, P. K. (2005). Crustal velocity structure across the Main Ethiopian Rift: Results from two-dimensional wide-angle seismic modelling. *Geophysical Journal International*, *162*(3), 994–1006. doi: 10.1111/j.1365-246X.2005.02710.x

Manighetti, I., Tapponnier, P., Gillot, P. Y., Jacques, E., Courtillot, V., Armijo, R., ... King, G. (1998). Propagation of rifting along the Arabia-Somalia Plate Boundary: Into Afar. *Journal of Geophysical Research: Solid Earth*, *103*(B3), 4947-4974. doi: 10.1029/97JB02758

Mazzarini, F., & Isola, I. (2010). Monogenetic vent self-similar clustering in extending continental crust: Examples from the East African Rift system. *Geosphere*, *6*(5), 567–582. doi: 10.1130/GES00569.1

Mazzarini, F., Le Corvec, N., Isola, I., & Favalli, M. (2016, 06). Volcanic field elongation, vent distribution, and tectonic evolution of a continental rift: The Main Ethiopian Rift example. *Geosphere*, *12*(3), 706-720. doi: 10.1130/GES01193.1

Mazzarini, F., Rooney, T. O., & Isola, I. (2013). The intimate relationship between strain and magmatism: A numerical treatment of clustered monogenetic fields in the Main Ethiopian Rift. *Tectonics*, *32*(1), 49–64. doi: 10.1029/2012TC003146

Mechie, J., Fuchs, K., & Altherr, R. (1994, September). The relationship between seismic velocity, mineral composition and temperature and pressure in the upper mantle—with an application to the Kenya Rift and its eastern flank. *Tectonophysics*, *236*(1-4), 453–464. doi: 10.1016/0040-1951(94)90189-9

Mendelson, K. S., & Cohen, M. H. (1982). The effect of grain anisotropy on the electrical properties of sedimentary rocks. *Geophysics*, *47*(2), 257–263. doi: 10.1190/1.1441332

Mickus, K., Tadesse, K., Keller, G., & Oluma, B. (2007). Gravity analysis of the main Ethiopian rift. *Journal of African Earth Sciences*, *48*(2), 59-69. (The East African Rift System: Dynamics, Evolution and Environment) doi: 10.1016/j.jafrearsci.2007.02.008

Ni, H., Keppler, H., & Behrens, H. (2011). Electrical conductivity of hydrous basaltic melts: Implications for partial melting in the upper mantle. *Contributions to Mineralogy and Petrology*, *162*(3), 637–650. doi: 10.1007/s00410-011-0617-4

Nicotra, E., Viccaro, M., Donato, P., Acocella, V., & De Rosa, R. (2021). Catching the Main

Ethiopian Rift evolving towards plate divergence. *Scientific Reports*, *11*(1), 1–16. doi: 10.1038/s41598-021-01259-6

Nigussie, W., Alemu, A., Muluneh, A. A., Mickus, K., & Muhabaw, Y. (2023, 02). Formation of magmatic segments within the Aluto-Gedemsa area, Main Ethiopian Rift. *Italian Journal of Geosciences*, *142*(1), 28-41. doi: 10.3301/IJG.2023.02

Omollo, P., Nishijima, J., Fujimitsu, Y., & Sawayama, K. (2022). Resistivity structural imaging of the Olkaria domes geothermal field in Kenya using 2D and 3D MT data inversion. *Geothermics*, *103*, 102414. doi: 10.1016/j.geothermics.2022.102414

Oppenheimer, C., Moretti, R., Kyle, P. R., Eschenbacher, A., Lowenstern, J. B., Hervig, R. L., & Dunbar, N. W. (2011). Mantle to surface degassing of alkalic magmas at Erebus volcano, Antarctica. *Earth and Planetary Science Letters*, *306*(3), 261-271. doi: 10.1016/j.epsl.2011.04.005

Peccerillo, A., Barberio, M. R., Yirgu, G., Ayalew, D., Barbieri, M., & Wu, T. W. (2003). Relationships between mafic and peralkaline silicic magmatism in continental rift settings: A petrological, geochemical and isotopic study of the Gedemsa volcano, Central Ethiopian Rift. *Journal of Petrology*, *44*(11), 2003–2032. doi: 10.1093/petrology/egg068

Pellerin, L., Johnston, J. M., & Hohmann, G. W. (1992). Evaluation of electromagnetic methods in geothermal exploration. In *Seg technical program expanded abstracts* (Vol. 1, pp. 405–408). Society of Exploration Geophysicists. doi: 10.1190/1.1822102

Pommier, A., & Garnero, E. J. (2014). Petrology-based modeling of mantle melt electrical conductivity and joint interpretation of electromagnetic and seismic results. *Journal of Geophysical Research: Solid Earth*, *119*(5), 4001-4016. doi: 10.1002/2013JB010449

Pride, S. (1994, Dec). Governing equations for the coupled electromagnetics and acoustics of porous media. *Phys. Rev. B*, *50*, 15678–15696. doi: 10.1103/PhysRevB.50.15678

Qi, Y., & Wu, Y. (2022). Electrical Conductivity of Clayey Rocks and Soils: A Non-Linear Model. *Geophysical Research Letters*, *49*(10), e2021GL097408. (e2021GL097408 2021GL097408) doi: 10.1029/2021GL097408

Regenspurg, S., Virchow, L., Wilke, F. D., Zimmer, M., Jolie, E., Hachenberger, A., ... Gizaw, B. (2022). Origin and migration of fluoride in the area of the Aluto Volcanic Complex (Main Ethiopian Rift). *Applied Geochemistry*, *146*, 105403. doi: 10.1016/j.apgeochem.2022.105403

Ronga, F., Lustrino, M., Marzoli, A., & Melluso, L. (2010). Petrogenesis of a basalt-

comendite-pantellerite rock suite: the Boseti Volcanic Complex (Main Ethiopian Rift). *Mineralogy and Petrology*, *98*(1-4), 227–243. doi: 10.1007/s00710-009-0064-3

Rooney, T., Furman, T., Bastow, I., Ayalew, D., & Yirgu, G. (2007). Lithospheric modification during crustal extension in the Main Ethiopian Rift. *Journal of Geophysical Research: Solid Earth*, *112*(B10). doi: 10.1029/2006JB004916

Rooney, T. O., Bastow, I. D., & Keir, D. (2011). Insights into extensional processes during magma assisted rifting: Evidence from aligned scoria cones. *Journal of Volcanology and Geothermal Research*, *201*(1-4), 83–96. doi: 10.1016/j.jvolgeores.2010.07.019

Rooney, T. O., Furman, T., Yirgu, G., & Ayalew, D. (2005). Structure of the Ethiopian lithosphere: Xenolith evidence in the Main Ethiopian Rift. *Geochimica et Cosmochimica Acta*, *69*(15), 3889–3910. doi: 10.1016/j.gca.2005.03.043

Rooney, T. O., Herzberg, C., & Bastow, I. D. (2012). Elevated mantle temperature beneath East Africa. *Geology*, *40*(1), 27–30. doi: 10.1130/G32382.1

Rung-Arunwan, T., Siripunvaraporn, W., & Utada, H. (2016). On the Berdichevsky average. *Physics of the Earth and Planetary Interiors*, *253*, 1–4. doi: 10.1016/j.pepi.2016.01.006

Rung-Arunwan, T., Siripunvaraporn, W., & Utada, H. (2022, April). The effect of initial and prior models on phase tensor inversion of distorted magnetotelluric data. *Earth, Planets and Space*, *74*(51), 1–24. doi: 10.1186/s40623-022-01611-8

Rychert, C. A., Hammond, J. O., Harmon, N., Michael Kendall, J., Keir, D., Ebinger, C., ... Stuart, G. (2012). Volcanism in the Afar Rift sustained by decompression melting with minimal plume influence. *Nature Geoscience*, *5*(6), 406–409. doi: 10.1038/ngeo1455

Samrock, F., Grayver, A., Dambly, M. L. T., Müller, M. R., & Saar, M. O. (2023). Geophysically guided well siting at the Aluto-Langano geothermal reservoir. *Geophysics*, *88*, 1-43. doi: 10.1190/geo2022-0617.1

Samrock, F., Grayver, A. V., Bachmann, O., Karakas, Ö., & Saar, M. O. (2021). Integrated magnetotelluric and petrological analysis of felsic magma reservoirs: Insights from Ethiopian rift volcanoes. *Earth and Planetary Science Letters*, *559*, 116765. doi: 10.1016/j.epsl.2021.116765

Samrock, F., Grayver, A. V., Cherkose, B., Kuvshinov, A., & Saar, M. O. (2020, 10). Aluto-Langano geothermal field, Ethiopia: Complete image of underlying magmatic-hydrothermal system revealed by revised interpretation of magnetotelluric data. In *Proceedings world geothermal congress (wgc 2020+1)* (p. 11054). Reykjavic, Iceland.

doi: 10.3929/ethz-b-000409980

Samrock, F., Grayver, A. V., Eysteinsson, H., & Saar, M. O. (2018). Magnetotelluric image of transcrustal magmatic system beneath the Tulu Moye geothermal prospect in the Ethiopian Rift. *Geophysical Research Letters*, *45*(23), 12–847. doi: 10.1029/2018GL080333

Samrock, F., Kuvshinov, A., Bakker, J., Jackson, A., & Fisseha, S. (2015). 3-D analysis and interpretation of magnetotelluric data from the Aluto-Langano geothermal field, Ethiopia. *Geophysical Journal International*, *202*(3), 1923–1948. doi: 10.1093/gji/ggv270

Samrock, F., Kuvshinov, A., Bakker, J., Jackson, A., Fisseha, S., staff of Addis Ababa University, & the Geological Survey of Ethiopia. (2010). *Magnetotelluric and vertical magnetic transfer functions acquired at the Aluto-Langano geothermal field, Ethiopia* [dataset]. (from the IRIS database, `http://ds.iris.edu/spud/emtf`) doi: 10.17611/DP/EMTF/ETHIOPIA/ETHZ

Schmucker, U., & Weidelt, P. (1975). Electromagnetic induction in the Earth. *Lecture Notes, Aarhus Univ., Denmark*.

Scott, S. W. (2020). Decompression boiling and natural steam cap formation in high-enthalpy geothermal systems. *Journal of Volcanology and Geothermal Research*, *395*, 106765. doi: 10.1016/j.jvolgeores.2019.106765

Sen, P., Scala, C., & Cohen, M. (1981). A self-similar model for sedimentary rocks with application to the dielectric constant of fused glass beads. *Geophysics*, *46*(5), 781–795. doi: 10.1190/1.1441215

Sruoga, P., Rubinstein, N., & Hinterwimmer, G. (2004, April). Porosity and permeability in volcanic rocks: a case study on the Serie Tobífera, South Patagonia, Argentina. *Journal of Volcanology and Geothermal Research*, *132*(1), 31–43. doi: 10.1016/S0377-0273(03)00419-0

Stuart, G., Bastow, I., & Ebinger, C. (2006). Crustal structure of the northern Main Ethiopian Rift from receiver function studies. *Geological Society, London, Special Publications*, *259*(1), 253-267. doi: 10.1144/GSL.SP.2006.259.01.20

Thybo, H., & Artemieva, I. (2013). Moho and magmatic underplating in continental lithosphere. *Tectonophysics*, *609*, 605–619. doi: 10.1016/j.tecto.2013.05.032

Tietze, K., Ritter, O., & Egbert, G. D. (2015). 3-d joint inversion of the magnetotelluric phase tensor and vertical magnetic transfer functions. *Geophysical Journal Interna-*

tional, *203*(2), 1128–1148. doi: 10.1093/gji/ggv347

Trainor-Guitton, W. J., Hoversten, G. M., Nordquist, G., & Intani, R. G. (2017). Value of mt inversions for geothermal exploration: Accounting for multiple interpretations of field data & determining new drilling locations. *Geothermics*, *66*, 13-22. doi: 10.1016/j.geothermics.2016.11.009

Tyburczy, J. A., & Waff, H. S. (1983, March). Electrical conductivity of molten basalt and andesite to 25 kilobars pressure: Geophysical significance and implications for charge transport and melt structure. *Journal of Geophysical Research, Solid Earth*, *88*(B3), 2413–2430. doi: 10.1029/JB088iB03p02413

van Wijk, J., & Blackman, D. (2007, 07). Development of en echelon magmatic segments along oblique spreading ridges. *Geology*, *35*(7), 599-602. doi: 10.1130/G23294A.1

Wannamaker, P. E., Hasterok, D. P., Johnston, J. M., Stodt, J. A., Hall, D. B., Sodergren, T. L., ... Unsworth, M. J. (2008). Lithospheric dismemberment and magmatic processes of the Great Basin–Colorado Plateau transition, utah, implied from magnetotellurics. *Geochemistry, Geophysics, Geosystems*, *9*(5). doi: 10.1029/2007GC001886

Weidelt, P. (1972, December). The inverse problem of geomagnetic induction. *Journal of Geophysics*, *38*, 257-289. doi: 10.1093/gji/35.1.379

Whaler, K., & Hautot, S. (2006). The electrical resistivity structure of the crust beneath the northern Main Ethiopian Rift. *Geological Society, London, Special Publications*, *259*(1), 293–305. doi: 10.1144/GSL.SP.2006.259.01.22

Wilks, M., Kendall, J.-M., Nowacki, A., Biggs, J., Wookey, J., Birhanu, Y., ... Bedada, T. (2017). Seismicity associated with magmatism, faulting and hydrothermal circulation at Aluto Volcano, Main Ethiopian Rift. *Journal of Volcanology and Geothermal Research*, *340*, 52-67. doi: 10.1016/j.jvolgeores.2017.04.003

Wilks, M., Rawlinson, N., Kendall, J. M., Nowacki, A., Biggs, J., Ayele, A., & Wookey, J. (2020). The coupled magmatic and hydrothermal systems of the restless Aluto Caldera, Ethiopia. *Frontiers in Earth Science*, *8*(October), 1–14. doi: 10.3389/feart.2020.579699

Wright, T. J., Ebinger, C., Biggs, J., Ayele, A., Yirgu, G., Keir, D., & Stork, A. (2006). Magma-maintained rift segmentation at continental rupture in the 2005 afar dyking episode. *Nature*, *442*(7100), 291–294. doi: 10.1038/nature04978

Yamaya, Y., Suzuki, Y., Murata, Y., Okamoto, K., Watanabe, N., Asanuma, H., ... Uchida, T. (2022). 3-D resistivity imaging of the supercritical geothermal system in the

Sengan geothermal region, NE Japan. *Geothermics*, *103*, 102412. doi: 10.1016/j.geothermics.2022.102412